J. Fluid Mech. (1985), *vol.* 157, *pp.* 327–357
Printed in Great Britain

Finite-difference simulation of nonlinear ship waves

By HIDEAKI MIYATA AND SHINICHI NISHIMURA†
Department of Naval Architecture, The University of Tokyo, Hongo, Bunkyo-ku, Tokyo 113

(Received 30 April 1984 and in revised form 28 January 1985)

A finite-difference solution method for nonlinear wave generation in the near field of ships of arbitrary three-dimensional configuration is developed. Momentum equations of finite-difference form in a fixed rectangular cell system are solved by a time-marching scheme. The exact inviscid free-surface condition is approximately satisfied at the actual location of the free surface, and the free-slip body boundary condition is implemented by use of approximation of the body configuration and a special pressure computation in body boundary cells. The degree of accuracy is raised by employing a variable-mesh system in the vertical direction. Computed results are presented for three hull forms: a mathematical and two practical hull forms. Agreement with experiment seems to be fairly good. In particular, the computed wave profiles and contour maps of bow waves show excellent resemblance to the measured ones, having some typical characteristics of nonlinear ship waves.

1. Introduction

Ships advancing on a steady straight course generate waves and suffer wave resistance. For high-speed ships more than half of the resistance is wave resistance, and a small modification in ship hull configuration gives rise to a remarkable increase or decrease of wave resistance. A properly designed bow bulb, for instance, can reduce it by 50%. This is why the problem of ship hull configuration of minimum wave resistance has attracted the attention of researchers in the field of hydrodynamics and applied mathematics for almost a hundred years.

Many wave-resistance theories have been proposed. It is almost impossible to count the number of papers that deal with wave-resistance problems of ships. However, the prediction of ship waves and wave resistance is not yet satisfactory. Theories so far developed can be relied on only when reinforced by the accumulated experimental results and the heuristic knowledge of designers. The inadequacy of the theories is assumed to result from the linearizing assumptions of the problem. In particular the linearization of the free-surface condition may not be appropriate for waves that show remarkable nonlinear characteristics, such as those generated by a blunt bow. An exceptional case is the Rankine source method by Gadd (1976), which is a kind of boundary-element method that satisfies the nonlinear free-surface condition on the exact location of the free surface. Another approach is to model the nonlinear behaviour of bow-waves, for instance the jet flow model by Dagan & Tulin (1972), but this kind of approach still needs much more refinement to attain the goal of the prediction of ship wave resistance.

The nonlinearity of ship waves has been experimentally investigated by many

† Present Address: Mitsubishi Heavy Industries, Kobe Shipyard, Wadamisaki, Hyogo-ku, Kobe 652.

researchers. Baba (1969) found the importance of the wave-breaking phenomenon, and Taneda (1974) noticed the existence of the so-called necklace vortices. Miyata (1980) advanced these studies and found the existence of a so-called free-surface shock wave. Waves in the near field of ships have many nonlinear characteristics with some similarity to nonlinear shallow-water waves and supersonic shock waves, such as the formation of a discontinuous steep wave slope. The nonlinear steep wave making is followed by the wave-energy-deficient phenomena of wave breaking and turbulence production, see Miyata & Inui (1984).

The theoretical explanation of the generation of steep nonlinear waves is the problem we deal with in this paper, and the succeeding much more complicated energy-deficient phenomena will be postponed to a future investigation. A finite-difference method similar to the MAC method of Welch *et al.* (1966) seems to be most effective for this nonlinear free-surface problem, since the nonlinear free-surface condition can be fulfilled at the actual location of the free surface by use of an ingenious technique. In this paper another finite-difference simulation method called TUMMAC (Tokyo University Modified Marker-And-Cell) method is developed for the ship-wave problem by synthesizing many finite-difference techniques and by improving them to suit the three-dimensional problem of ships advancing on the free surface. In the following sections, the computational method is described together with the complicated treatment of body boundary conditions, and the computed results are compared with experimental results and discussed.

2. Computational method

2.1. *Solution procedure*

A ship is considered to be a fixed floating body placed in a uniform stream. The ship-wave problem is solved by computing the flow field around a ship. Since ship waves have many nonlinear characteristics, linearizing postulations must be avoided as far as possible. Therefore the Navier–Stokes (NS) equations are employed as governing equations. However, since we suppose that the viscous effects on both the free surface and body surface are safely neglected for free-surface waves of ships, inviscid boundary conditions are imposed on these boundaries. In most cases the viscous term of the NS equations can be ignored by setting the kinematic viscosity at zero. Hence in reality the Euler equations are used, while the solution procedure is explained by the NS equations.

The basic concept of the solution algorithm is similar to the MAC method developed by Welch *et al.* (1966) and its improved version by Hirt & Nichols (1981). The momentum and continuity equations are represented in finite-difference form and solved through the solution procedure for an initial and boundary-value problem. For the computation of ship waves the water flow is accelerated from the rest condition by time marching until a steady state is reached after the flow acceleration has ceased.

A Cartesian coordinate system is employed, in which the x-axis is parallel to a ship centreline, its origin being at the forward end of a ship, the y-axis is oriented transversely, and the z-axis is oriented vertically, positive upward. The undisturbed free surface is the plane at $z = 0$, and the ship advances in the negative x-direction. A staggered semi-variable mesh system is used. Dimensions of each rectangular cell are DX, DY, and DZ in the x, y, z directions, respectively, and DX and DY are common to all the cells, while DZ varies with respect to the z-coordinate. DZ is smallest near the free surface where the velocity gradient may be greatest. Velocities are defined on six surfaces of a cell and pressure at the centre of a cell, as shown in figure 1.

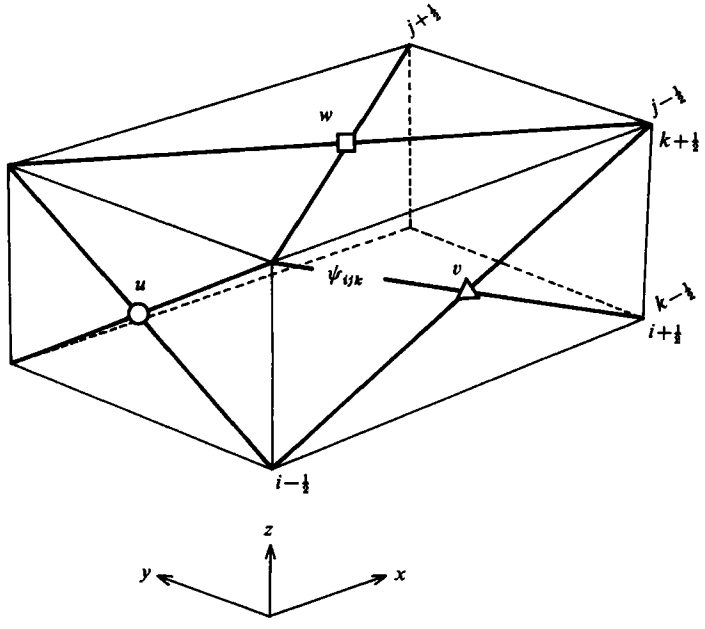

FIGURE 1. Staggered mesh system.

The NS equations are represented in a finite-difference form by forward differencing in time and centred differencing in space except for the convective terms:

$$\left.\begin{aligned} u^{n+1}_{i+\frac{1}{2},j,k} &= \xi_{i+\frac{1}{2},j,k} - \frac{\Psi_{i+1,j,k}-\Psi_{i,j,k}}{\mathrm{D}X}\,\mathrm{D}T, \\ v^{n+1}_{i,j+\frac{1}{2},k} &= \eta_{i,j+\frac{1}{2},k} - \frac{\Psi_{i,j+1,k}-\Psi_{i,j,k}}{\mathrm{D}Y}\,\mathrm{D}T, \\ w^{n+1}_{i,j,k+\frac{1}{2}} &= \zeta_{i,j,k+\frac{1}{2}} - \frac{\Psi_{i,j,k+1}-\Psi_{i,j,k}}{\mathrm{D}Z_k}\,\mathrm{D}T, \end{aligned}\right\} \tag{1}$$

where

$$\left.\begin{aligned} \xi_{i+\frac{1}{2},j,k} &= u_{i+\frac{1}{2},j,k} - \mathrm{D}T.UC_{i+\frac{1}{2},j,k} + \nu\,\mathrm{D}T\left[\frac{u_{i+\frac{3}{2},j,k}+u_{i-\frac{1}{2},j,k}-2u_{i+\frac{1}{2},j,k}}{\mathrm{D}X^2}\right. \\ &\quad + \frac{u_{i+\frac{1}{2},j+1,k}+u_{i+\frac{1}{2},j-1,k}-2u_{i+\frac{1}{2},j,k}}{\mathrm{D}Y^2} \\ &\quad \left. + \frac{u_{i+\frac{1}{2},j,k+1}+u_{i+\frac{1}{2},j,k-1}-2u_{i+\frac{1}{2},j,k}}{\mathrm{D}Z_k^2}\right], \\ \eta_{i,j+\frac{1}{2},k} &= v_{i,j+\frac{1}{2},k} - \mathrm{D}T.VC_{i,j+\frac{1}{2},k} + \nu\,\mathrm{D}T[\ldots], \\ \zeta_{i,j,k+\frac{1}{2}} &= w_{i,j,k+\frac{1}{2}} - \mathrm{D}T.WC_{i,j,k+\frac{1}{2}} + \nu\,\mathrm{D}T[\ldots] + g. \end{aligned}\right\} \tag{2}$$

Here u, v, w are velocity components in the x, y, z directions, respectively, and Ψ is pressure divided by the density of water. $\mathrm{D}X$, $\mathrm{D}Y$, $\mathrm{D}Z_k$ are the spacing of velocity and pressure points in each direction, namely the dimensions of a cell, and $\mathrm{D}T$ is the time increment. Subscripts i, j, k are used for the x, y, z locations, respectively, and superscripts for time level. The superscript n is usually dropped. In (2) UC, VC and

WC are convective terms in finite-difference form more fully described in §2.2, and ν is the kinematic viscosity.

By use of the continuity equation the following Poisson equation for pressure is derived:

$$\Psi_{i,j,k} = \frac{1}{2}\left\{\frac{1}{DX^2}+\frac{1}{DY^2}+\frac{1}{DZ_{k-\frac{1}{2}}\,DZ_{k+\frac{1}{2}}}\right\}^{-1}\left[\frac{\Psi_{i+1,j,k}+\Psi_{i-1,j,k}}{DX^2}\right.$$
$$\left.+\frac{\Psi_{i,j+1,k}+\Psi_{i,j-1,k}}{DY^2}+\frac{DZ_{k-\frac{1}{2}}\,\Psi_{i,j,k+1}+DZ_{k+\frac{1}{2}}\,\Psi_{i,j,k-1}}{DZ_{k-\frac{1}{2}}\,DZ_{k+\frac{1}{2}}\,\frac{1}{2}(DZ_{k-\frac{1}{2}}+DZ_{k+\frac{1}{2}})}-R_{i,j,k}\right], \quad (3)$$

where

$$R_{i,j,k} = \frac{\xi_{i+\frac{1}{2},j,k}-\xi_{i-\frac{1}{2},j,k}}{DT.DX}+\frac{\eta_{i,j+\frac{1}{2},k}-\eta_{i,j-\frac{1}{2},k}}{DT.DY}+\frac{\zeta_{i,j,k+\frac{1}{2}}-\zeta_{i,j,k-\frac{1}{2}}}{DT.DZ_k} \quad (4)$$

and

$$DZ_{k\pm\frac{1}{2}} = \tfrac{1}{2}(DZ_k+DZ_{k\pm1}). \quad (5)$$

Since variable mesh spacing in the z-direction is used, (3) is a little complicated and the degree of accuracy of the above finite-difference approximation of the Poisson equation is lower than the case of constant spacing. However, the overall accuracy of the solution may be increased by allotting very fine cells where fluid motion is most important, as will be demonstrated below.

Equation (3) is iteratively solved by a simultaneous iterative method through the following equation, which is in a simplified form assuming that the vertical spacing DZ_k varies linearly:

$$\Psi^{m+1}_{i,j,k} = \Psi^{m}_{i,j,k}-\frac{\omega[D^m_{i,j,k}]}{2DT\{1/DX^2+1/DY^2+1/(DZ_{k-\frac{1}{2}}\,DZ_{k+\frac{1}{2}})\}}, \quad (6)$$

where

$$D^m_{i,j,k} = \frac{u^m_{i+\frac{1}{2},j,k}-u^{m+1}_{i-\frac{1}{2},j,k}}{DX}+\frac{v^m_{i,j+\frac{1}{2},k}-v^{m+1}_{i,j-\frac{1}{2},k}}{DY}+\frac{w^m_{i,j,k+\frac{1}{2}}-w^{m+1}_{i,j,k-\frac{1}{2}}}{DZ_k}. \quad (7)$$

Here, superscripts denote iterative number and ω is a relaxation factor. D is the divergence of a cell as defined above.

At every time step the pressure field is determined from the fixed velocity field under various boundary conditions. The new pressure field gives a new velocity field by advancing one time step using (1). The free-surface configuration is derived from the movement of marker particles located on the free surface. The time marching is advanced until a steady state is reached.

2.2 *Finite differencing of the convective term and stability considerations*

For the finite-difference representation of the convective terms *UC*, *VC* and *WC*, a combination of second-order upstream differencing (donor-cell method) and centred differencing is employed following Hirt, Nichols & Romero (1975). The second-order error of the donor-cell method that causes numerieal dissipation is compensated by the same-order error of the centred differencing with opposite sign that causes numerical instability.

The x-directional convective term *UC* at $i+\frac{1}{2}$, for instance, is written as

$$UC_{i+\frac{1}{2},j,k} = \frac{(u^2)_{i+1,j,k}-(u^2)_{i,j,k}}{DX}+\frac{(uv)_{i+\frac{1}{2},j+\frac{1}{2},k}-(uv)_{i+\frac{1}{2},j-\frac{1}{2},k}}{DY}$$
$$+\frac{(uw)_{i+\frac{1}{2},j,k+\frac{1}{2}}-(uw)_{i+\frac{1}{2},j,k-\frac{1}{2}}}{DZ_k}. \quad (8)$$

The first term, for instance, is calculated from the equation:

$$\frac{(u^2)_{i+1,j,k}-(u^2)_{i,j,k}}{DX} = \tfrac{1}{4}DX[\{(u_{i+\frac{1}{2},j,k}+u_{i+\frac{3}{2},j,k})^2-(u_{i-\frac{1}{2},j,k}+u_{i+\frac{1}{2},j,k})^2\} + \alpha\{|u_{i+\frac{1}{2},j,k}+u_{i+\frac{3}{2},j,k}|(u_{i+\frac{1}{2},j,k}-u_{i+\frac{3}{2},j,k}) - |u_{i-\frac{1}{2},j,k}+u_{i+\frac{1}{2},j,k}|(u_{i-\frac{1}{2},j,k}-u_{i+\frac{1}{2},j,k})\}]. \quad (9)$$

Here α is a combination factor; for centred differencing $\alpha = 0$, and for the donor-cell method $\alpha = 1$.

Since a variable-mesh system is used, the space differencing is not equivalent to the centred differencing nor the donor-cell method in a strict sense. Therefore the degree of accuracy is lowered by the variable-mesh system. However, by the employment of locally very fine cells the overall accuracy can be increased as demonstrated below.

For the stability consideration Neumann's method (Roache 1976) is used after linearizing the convective and diffusive terms and dropping the pressure-gradient terms together with the gravitational term of the NS equations. Then the approximate condition is obtained as follows:

$$(C_x+C_y+C_z)^2 \leqslant \alpha(C_x+C_y+C_z)+2(d_x+d_y+d_z) \leqslant 1. \quad (10)$$

Here C_x, C_y, C_z are Courant numbers and d_x, d_y, d_z are diffusion numbers defined as

$$\left.\begin{aligned} C_x &= \frac{DT\,u}{DX}, \quad C_y = \frac{DT\,v}{DY}, \quad C_z = \frac{DT\,w}{DZ}, \\ d_x &= \frac{DT\,\nu}{DX^2}, \quad d_y = \frac{DT\,\nu}{DY^2}, \quad d_z = \frac{DT\,\nu}{DZ^2}. \end{aligned}\right\} \quad (11)$$

Equation (10) is separated to give

$$(C_x+C_y+C_z) \leqslant \alpha < 1, \quad (12)$$

$$\nu \leqslant \frac{1-\alpha(C_x+C_y+C_z)}{2DT(1/DX^2+1/DY^2+1/DZ^2)}. \quad (13)$$

Equation (12) gives conditions for the combination factor and Courant number, and (13) the upper limit of the kinematic viscosity. Since these stability conditions are based on gross assumptions, they are approximate necessary conditions, and they do not always guarantee the stability of solutions. In fact instability of solution often occur on the body surface and the free surface where nonlinear fluid motions are initiated. To secure real stability careful treatment is necessary there, as will be described in the next section.

2.3. *Approximation of ship hull configuration*

An arbitrary three-dimensional body boundary condition is developed here in the framework of the rectangular-cell system. The alternative is the employment of a body-fitted coordinate system, in which the implementation of body boundary conditions is attained without difficulty. A body-fitted coordinate system has been successfully used many times, especially in two-dimensional problems. However, in the present three-dimensional flow problem that contains a free surface its employment may give rise to some difficulties. For instance, the coordinate transformation needs to be conducted at every time step owing to the deformation of the free-surface configuration.

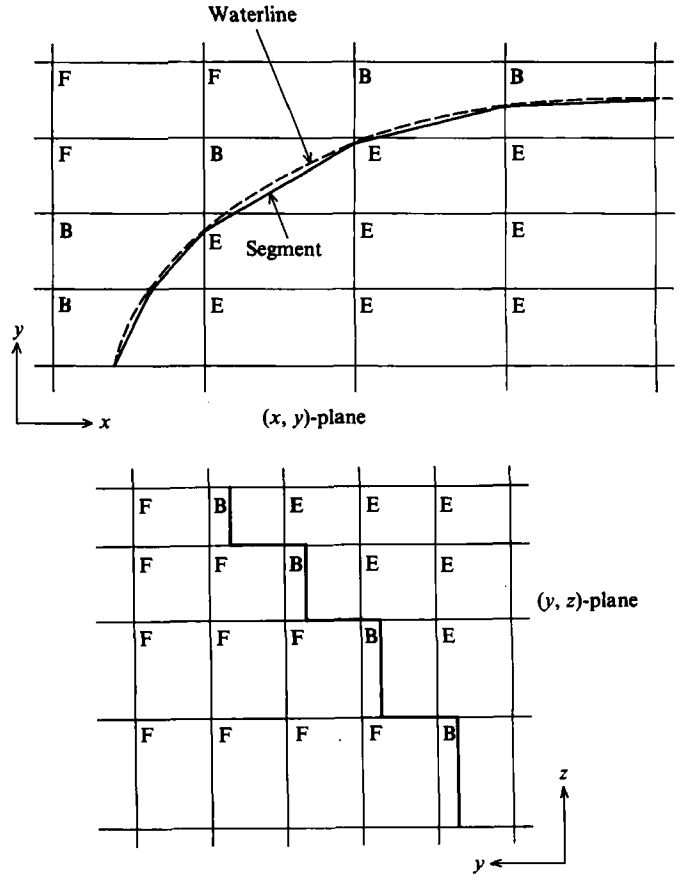

FIGURE 2. Simplification of body configuration and flagging.

The employment of a fixed rectangular-cell system concentrates the difficulties of the solution procedure on the implementation of body boundary conditions. For the computation of fluid motion on the very complicated body configuration of a ship some simplification is necessary. A ship body is made of horizontal curves in (x, y)-planes (waterlines) and vertical curves in (y, z)-planes (framelines). The former require more careful treatment than the latter, since they are more sensitive to wave resistance. A waterline is approximated by a succession of straight segments as shown in figure 2. The waterline on the horizontal plane that contains the centres of cells is used to determine the segments, and the vertical variation of frameline within a cell height is ignored. Then the body surface comprises vertical and horizontal plane panels.

All the cells are flagged and classified into full-of-fluid cells (F-cells), body boundary cells (B-cells) and empty cells (E-cells). A B-cell is a cell (i) that contains both fluid and body, (ii) that contains a fluid portion of more than a quarter of the cell volume, and (iii) that has at least one velocity not determined by (1). An F-cell neighbouring B- and E-cells is sometimes defined as B-cell so that B-cells are continuously distributed along waterlines, even though the above condition (i) is violated. Some examples of flagging are shown in figure 2. The cell denoted K is a body boundary cell, in which one vertical velocity is set at zero and so the other complicated procedures for a B-cell are not necessary.

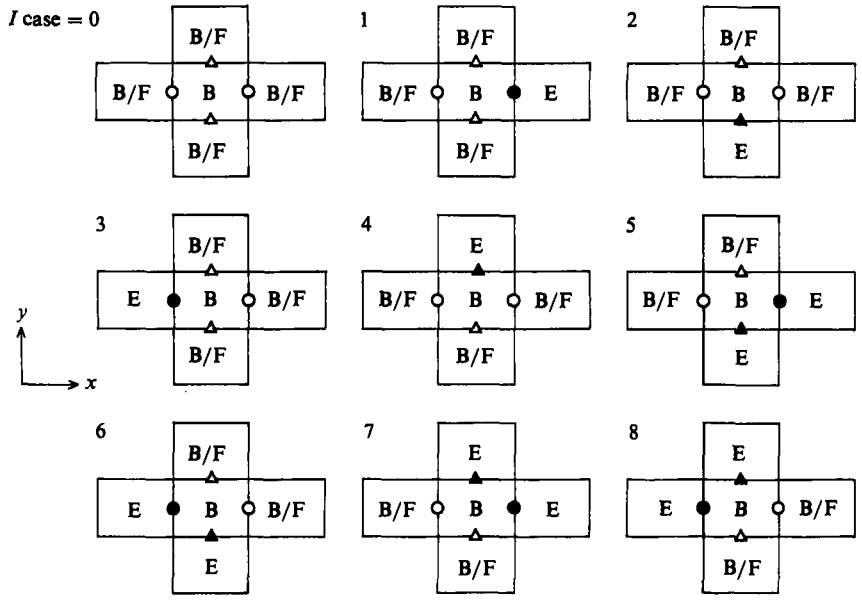

FIGURE 3. The B-cells on horizontal plane: ○ △, velocity facing B/F-cell; ● ▲, velocity facing E-cell.

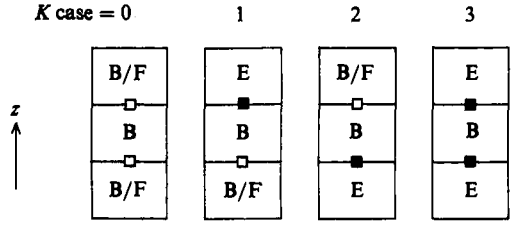

FIGURE 4. The B-cells on vertical plane: □, velocity facing B/F-cell; ■, velocity facing E-cell.

A B-cell has six neighbouring cells, either F-, B- or E-cells. The procedure to fulfil the body boundary conditions in a B-cell depends on the kind of neighbouring cells, since an E-cell does not have pressure and the velocity on the plane facing an E-cell cannot be computed by momentum equations. Then each B-cell is classified into nine horizontal cases shown in figure 3 and four vertical cases shown in figure 4. The velocities shown as black marks are not normally computed.

2.4. *Body boundary condition*

It is possible to apply a free-slip body boundary condition, since the cell size cannot be so small as to resolve viscous motion in a boundary layer. The Reynolds number that corresponds to the model ship length and its speed of advance is greater than 10^6. For a free-slip condition the following must occur: (i) the velocity normal to a body surface is zero; (ii) the tangential velocity does not have normal gradient; and (iii) the divergence of a B-cell is zero.

The procedure to fulfil the above three conditions is explained here for the most typical case when I case = 5 and K case = 0. The body configuration is simplified so that the body surface is made of vertical and horizontal plane panels as seen in

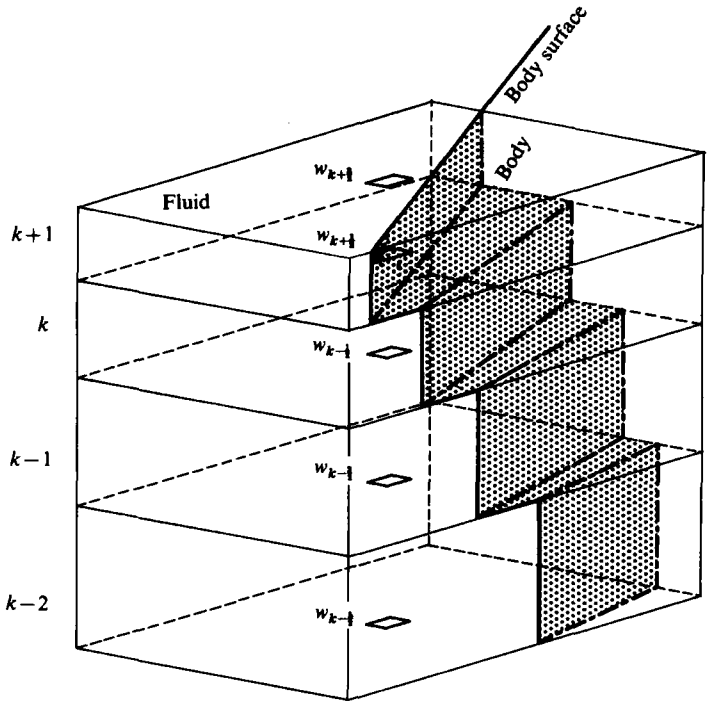

FIGURE 5. Simplified body surface and velocity points of w.

figure 5. Then the velocity normal to the body surface is either horizontal or vertical. The horizontal normal velocity is set at zero through adjustment of the pressure in the B-cell and surrounding cells by iteration, and the vertical normal velocity is set either at zero or given a certain value depending on the area of a horizontal plane of the B-cell across which fluid can pass vertically.

In the course of solving the Poisson equation iteratively the following equation is used instead of (6) for an F-cell, following Viecelli (1971):

$$\Psi^{m+1}_{i,j,k} = \Psi^{m}_{i,j,k} - \frac{\omega}{2\delta\,\mathrm{D}T}(\boldsymbol{V}_{\mathrm{p}}\cdot\boldsymbol{n}). \tag{14}$$

Here, $\boldsymbol{V}_{\mathrm{p}}$ and $\boldsymbol{n}$ are the fluid velocity vector at the centre of the segment and a unit outward normal vector of a segment respectively, as shown in figure 6. δ is a mesh parameter and taken to be $1/\mathrm{D}X+1/\mathrm{D}Y+1/\mathrm{D}Z_k$. Equation (14) shows that the horizontal normal velocity becomes zero when the pressure converges. Simultaneously the zero-divergence condition of the fluid portion of the B-cell is attained when the divergence of the full volume of the B-cell is set at zero since fluid does not move across the segment.

Two velocities $V1$ and $U2$ in figure 6, which are not determined by momentum equations, are set so that the zero-divergence condition of the full volume of the B-cell and the condition of no gradient of tangential velocity are fulfilled. They are set as follows in the iterative process of adjusting pressure:

$$U2 = U1+a, \quad V1 = V2+b, \tag{15}$$

where

$$\frac{a}{\mathrm{D}X}+\frac{b}{\mathrm{D}Y}+\frac{W2.SF2-W1.SF1}{\mathrm{D}Z} = 0. \tag{16}$$

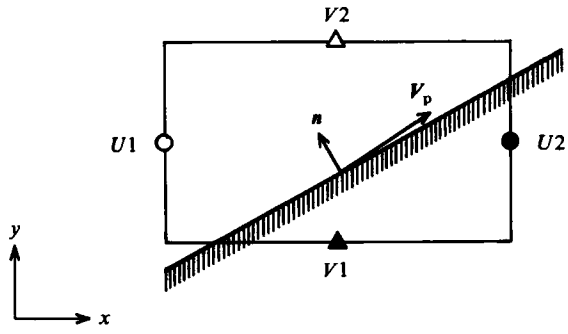

FIGURE 6. Definition sketch for body boundary condition on horizontal plane.

Here, $W1$ and $W2$ are vertical velocities on lower and upper surfaces of the B-cell and $SF1$ and $SF2$ are dimensionless areas of the fluid portion of the surfaces, across which fluid can vertically pass. The values of additional velocities a and b are determined by the zero-divergence condition expressed in (15) and (16) and the additional condition that the velocity which a and b induce at the centre of the segment is normal to the segment. Thus, the zero-divergence condition and no-normal-gradient-of-tangential-velocity condition are approximately satisfied in the iterative procedure.

2.5. *Free-surface condition*

The free-surface condition is also most important in the nonlinear free-surface problem of ship waves. Let the location of the free surface be $z = \zeta$, and then the inviscid free-surface conditions on this location are

$$\Psi = \Psi_0, \tag{17}$$

$$\frac{\mathrm{D}\zeta}{\mathrm{D}t} \equiv \frac{\partial \zeta}{\partial t} + u\frac{\partial \zeta}{\partial x} + v\frac{\partial \zeta}{\partial y} - w = 0. \tag{18}$$

Here Ψ_0 is the atmospheric pressure P_0 divided by the density of water. Equations (17) and (18) are the dynamic and kinematic conditions respectively, and they are exact when the viscous stress and the surface tension on the free surface are neglected. They are safely assumed to be zero in the present high-Froude-number-flow problem.

For the fulfilment of condition (17) the 'irregular star' of Chan & Street (1970) is used. It is another finite-difference representation of the Poisson equation with variable spacing, i.e. η_1–η_6 as follows:

$$\Psi_{i,j,k} = \frac{\eta_1\eta_2\eta_3\eta_4\eta_5\eta_6}{\eta_1\eta_2\eta_3\eta_4 + \eta_3\eta_4\eta_5\eta_6 + \eta_1\eta_2\eta_5\eta_6} \times \left[\frac{\eta_2\Psi_1 + \eta_1\Psi_2}{\eta_1\eta_2(\eta_1+\eta_2)} + \frac{\eta_4\Psi_3 + \eta_3\Psi_4}{\eta_3\eta_4(\eta_3+\eta_4)} + \frac{\eta_6\Psi_5 + \eta_5\Psi_6}{\eta_5\eta_6(\eta_5+\eta_6)} - \tfrac{1}{2}R_{i,j,k}\right]. \tag{19}$$

Here Ψ_1–Ψ_6 are the pressures at the end of the six legs η_1 to η_6, respectively. When the free surface is closer to one pressure point than the neighbouring pressure point, the pressure is set at Ψ_0 and the leg length is the distance to the free surface. Thus the computation of pressure in cells near the free surface by (19) is continued from the normal pressure computation at each iterative step.

The kinematic condition (18) is fulfilled by the use of marker particles on the free

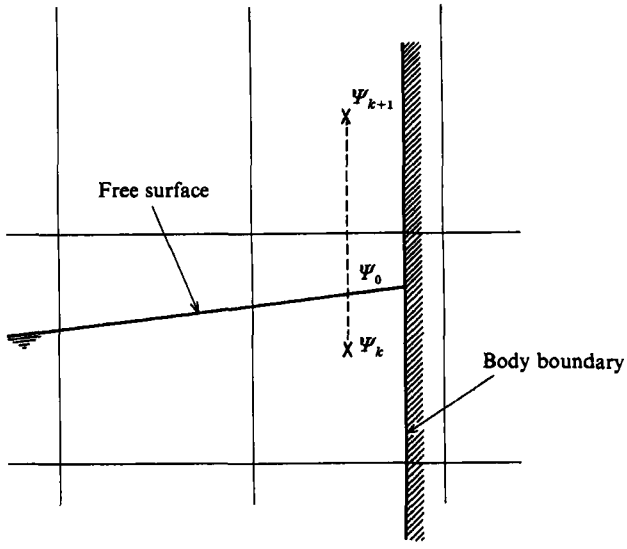

FIGURE 7. Definition sketch for the treatment of a boundary cell containing a free surface.

surface. The marker particles move in a Lagrangian manner and their new location gives the new free-surface configuration. Only one marker particle is allotted to each free surface cell. The initial location of marker particles is iteratively calculated so that the new location is straight above the centre of the cells. This is convenient for determining and drawing the new wave configuration on an (x, y)-plane.

In most of the solution procedures for body–wave interaction problems the singularity at the intersection of the free surface and the body surface gives rise to analytical difficulties and sometimes it is the cause of instability of the solution. Special consideration is often necessary here in order to have a satisfactory stable solution. For example Lin, Newman & Yue (1984) recently discussed this problem in the computation of waves generated by a wavemaker using a boundary-element method.

In the present method a special treatment is introduced in the pressure computation of a boundary cell that contains a free surface. The pressure Ψ_{k+1} of the cell above such a B-cell, shown in figure 7, is linearly extrapolated from Ψ_k of the B-cell and zero-pressure Ψ_0 on the free surface so that the velocity w on the upper surface of the B-cell is evaluated. Also, in the computation of Ψ_k by an iterative solution procedure for the Poisson equation the relaxation factor ω is reduced taking into account the distance between the points Ψ_k and Ψ_0 in figure 7, see Nichols & Hirt (1971). Assume that this vertical distance is s; then the reduced relaxation factor ω' is derived as

$$\omega' = \frac{4\omega}{4-\omega(1-\mathrm{DZ}/s)}. \tag{20}$$

Other computations are performed in the same manner with a normal B-cell. The above procedure is necessitated by not only the singularity at the intersection but also the geometrical irregularity of a cell that contains both a free surface and a body surface, which is because of the inflexible rectangular-cell system. To secure the stability of the solution these special treatments are necessary: without them the

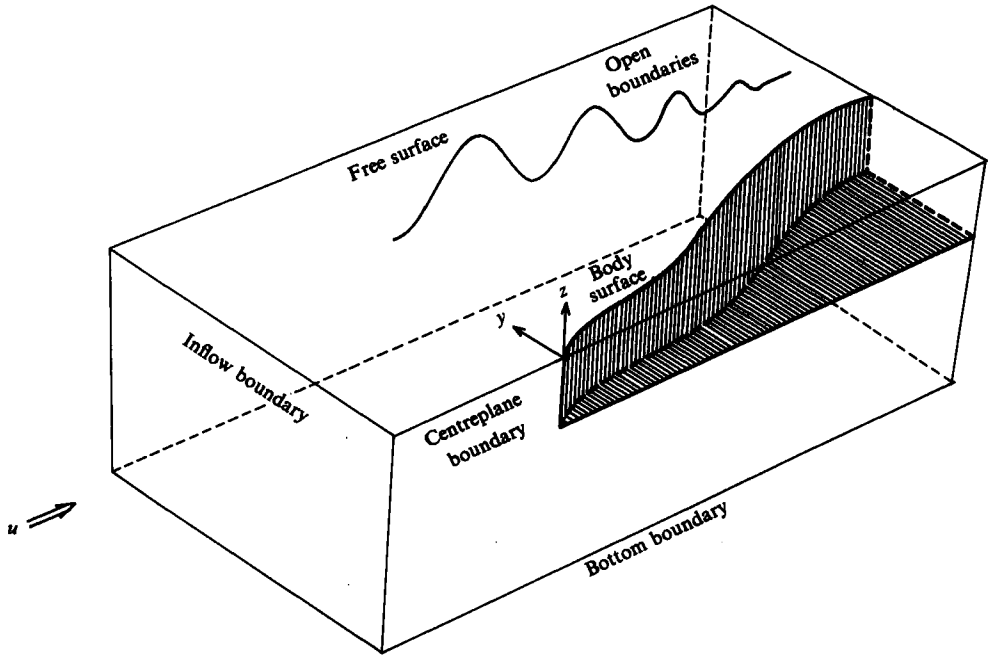

FIGURE 8. Computational domain and boundaries.

divergence of the solution occasionally emerges from the body surface. The above approximate treatment may influence the accuracy of the solution. However, the error due to this approximation can be reduced by using a fine cell division near the free surface.

2.6. *Other boundary conditions*

The computational domain is bounded by a centreplane boundary, an inflow boundary, a bottom boundary, a side boundary, an outflow boundary, a body boundary and a free surface as seen in figure 8.

The centreplane bisects the cells in which pressure is first renewed. Symmetry conditions for pressure, velocity v and convective term η are imposed as

$$\Psi_{i,1,k} = \Psi_{i,3,k}, \tag{21a}$$

$$v_{i,\frac{3}{2},k} = -v_{i,\frac{5}{2},k}, \tag{21b}$$

$$\eta_{i,\frac{3}{2},k} = -\eta_{i,\frac{5}{2},k}. \tag{21c}$$

At the inflow boundary a uniform distribution of u is imposed. This is easily accepted when the disturbance due to a ship is scarcely noticeable at the inflow boundary. The bottom boundary is usually so deep that the fluid motion is very gentle. Then, hydrostatic pressure is given there, and velocity w is computed through the momentum equation and the zero-divergence condition.

The condition at the open boundary is also important. It is usually considered that the strict implementation of this condition is very difficult, and a number of studies have been done to improve its numerical treatment. An improper condition gives rise to unfavourable results, such as wave reflection or divergence of the solution at the open boundary.

There are two open boundaries on which a radiation condition must be satisfied.

At the side boundary all the variables are set equal to the inner values so that their gradient in the direction normal to the boundary is zero. At the rear open boundary their gradient along the local flow direction is set at zero. These simple conditions work well, partly attributable to the transportive property of the donor-cell method.

3. Computed results

3.1. *Condition of computation*

Three ship models with a three-dimensional configuration were chosen for the computation. One is a simple mathematical model called Wigley's hull, the surface of which is made of parabolic curves as defined by

$$y = \tfrac{1}{2}B\left\{1-\left(\frac{2x}{L}\right)^2\right\}\left\{1-\left(\frac{z}{d}\right)^2\right\}. \tag{22}$$

Here L, B and d are ship-model length, breadth and draught (depth below the undisturbed free surface), respectively. The other two are practical ship models of a bulk carrier of 26000 deadweight tonnage which is equipped with a bow bulb and a tanker of 200000 deadweight tonnage which has a normal bow form without a bulb, named M55F0 and M57F0 respectively. Only the lightly loaded condition (ballast condition) is considered for M55F0, while both ballast and full-load conditions are considered for M57F0. The principal characteristics of the three ship models are listed in table 1.

In order to ascertain the effect of cell size on the accuracy of the solution some numerical tests were performed with the fore part of the Wigley's hull at $Fn = 0.289$. The results are shown in figure 9 in the form of a wave contour map. In case (*a*) where the longitudinal spacing DX is 2% of ship length the waves are significantly attenuated, having inadequate maximum wave height, namely only about 65% of the measured value. In case (*b*) where DX is reduced to 1% of ship length the outward extension of wave contours and the wave formation behind the wave crest are still insufficient in comparison with the experimental result shown in figure 14, although the maximum wave height almost reaches the experimental value. The use of the variable-mesh system in the vertical direction with a very fine cell spacing near the free surface considerably increases the accuracy, as seen in case (*c*).

By further reducing the cell size improvement of accuracy tends to be considerably reduced and eventually ceases, as is described in §3.2 and figure 15. By rule of thumb the horizontal spacing of a cell must not be greater than 1% of ship length for the present method. Numerical tests show that for ship models where the waterline curvature is concentrated on the fore and aft parts, with a long parallel middle body such as M55F0 and M57F0, the horizontal spacing must be smaller than 1% of ship length, but it should not be smaller than 0.5% from an economical point of view, since the improvement in accuracy is small.

The computation conditions are listed in table 2. Only the fore parts of the ship models are considered for the Wigley's hull and M57F0, but the full length of the model is considered for M55F0. One Froude number is chosen for each ship model: a relatively high one for the very fine hull form of the Wigley's hull and one that corresponds to their operation speed for the two practical hull forms. Since the wave elevation by M57F0 at a very low Froude number is expected to be much smaller than by M55F0 that advances at a higher Froude number, the cell size for M57F0 is taken to be smaller than M55F0. An exceptionally small cell size is used for the

Name of hull	Wigley's hull	M55F0	M57F0	
Type of hull	Horizontally and vertically parabolic	Practical bulk carrier	Practical tanker	
			Ballast	Full-load
Length L (m)	2.500	3.000	2.800	
Breadth B (m)	0.250	0.497	0.509	
Draft d (m)	0.156	0.090	0.0663	0.1664
Computed Froude number	0.289	0.180	0.150	

TABLE 1. Principal particulars of ship models

Wigley's hull to discover the ultimate degree of accuracy that would be attained by the present method.

The spacing in z-direction DZ is variable. It is linearly decreased from the bottom of the computational domain to the undisturbed free surface as seen in figure 11. Above the undisturbed free surface DZ is constant. For the consideration of the stability conditions expressed by (12) and (13) the smallest DZ is used. Some drawings of cell division are presented in figures 10 and 11 for the Wigley's hull, in figures 17 and 18 for M55F0.

The kinematic viscosity is set at zero or the actual value but the difference is assumed to be negligibly small, since a free-slip body boundary condition is employed and the diffusion terms are expected to influence the waves only very slightly.

3.2. *Computed results*

The time-evolutional development of waves around the fore part of the Wigley's hull is shown in figure 12, and the perspective view of wave configuration at the final steady state is in figure 13. The wave height is made dimensionless by the water head of uniform stream H, equal to $U^2/2g$. The velocities in the computational domain are uniformly accelerated for 500 time-steps from zero to 1.429 m/s.

The computed wave-contour map at the completely steady state is compared with measurements in figure 14. The fluctuations of the measured contours are presumably attributable to the error in measurement and to the inadequate contour plotting program. The agreement is satisfactory especially in the angle of wave crest. However, it is also noted that the computed waves show attenuation in wave height in the region far from the body surface, which is presumably caused by numerical dissipation. The computed wave profile on the body surface is compared with measurements in figure 15. Since the modified Rankine source method proposed by Dawson (1979) which applies a linearized free-surface condition is considered to be one of the most successful methods, it was recently used by Ogiwara (1983) for a Wigley's hull and the computed wave profile is shown in figure 15. However, the superior accuracy of the present method is obvious. In spite of the Wigley's hull having a very fine configuration which should result in insignificant nonlinearity of the waves a theory that linearizes the free-surface condition does not give satisfactory agreement. This seems to imply that implementation of the nonlinear free-surface condition is of importance for the evaluation of ship waves and wave resistance. The computed result with a somewhat coarser cell system is also shown in figure 15. It

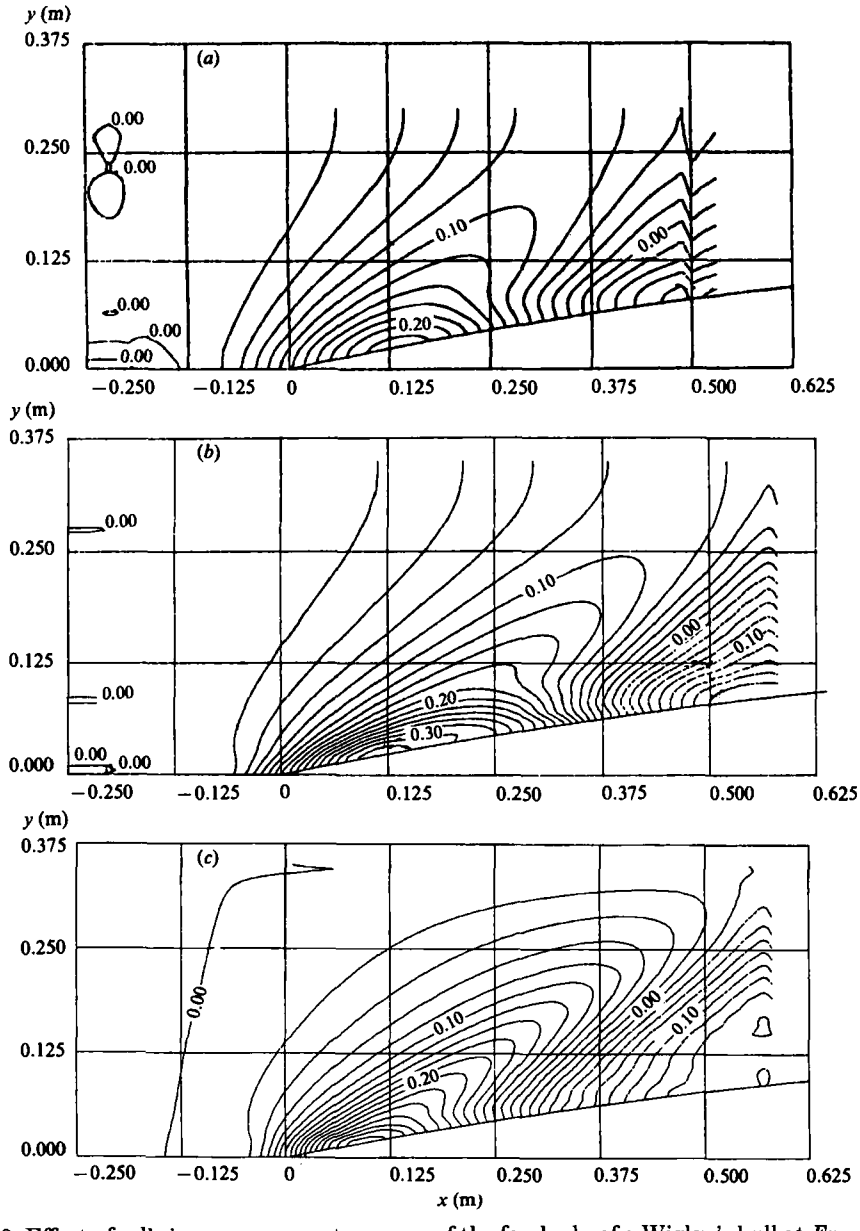

FIGURE 9. Effect of cell size on wave-contour map of the forebody of a Wigley's hull at $Fn = 0.289$: (*a*) $DX \times DY \times DZ = 50 \times 10 \times 31.2$ mm; (*b*) $25 \times 10 \times 31.2$ mm; (*c*) $25 \times 10 \times 8.9 \sim 58$ mm.

is noted that the improvement of the degree of accuracy by the reduction of grid spacing from 25 mm to 10 mm is rather slight. The degree of accuracy of the present method stops improving when the spacing approaches 0.5% of ship length. The fluctuation of the computed wave profile on the crest seems to be due to numerical instability, but it has negligible influence since it is restricted to a small region.

Velocity-vector fields of velocity components on two (y, z)-planes are shown in figure 16. The present finite-difference method gives, as a matter of course, solutions of all the velocity components and pressure over all the computational domain, and

	Name of hull			
			M57F0	
	Wigley's hull	M55F0	Ballast	Full-load
Domain of computation				
Length (m)	0.850	4.480	1.122	
Breadth (m)	0.350	0.900	0.495	
Depth (m)	0.313	0.393	0.210	0.393
Cell size				
DX (mm)	10	20	16.5	
DY (mm)	7	20	16.5	
DZ (mm)	6.3 ~ 35.4	12 ~ 42	7.4 ~ 25.1	8.2 ~ 44.1
Approximate number of used cell	59000	100000	29000	33000
Time increment DT (s)	0.00164	0.00461	0.00338	0.00423
Time steps for acceleration	500	300	300	
Total time steps	800	600	800	
Combination factor α	0.5	0.5	0.5	
Relaxation factor ω	1.5	1.5	1.5	
Kinematic viscosity ν (m^2/s)	0	1.139×10^{-6}	0	
Froude number Fn	0.289	0.180	0.150	
Speed of advance (m/s)	1.429	0.976	0.786	

TABLE 2. Conditions of computation

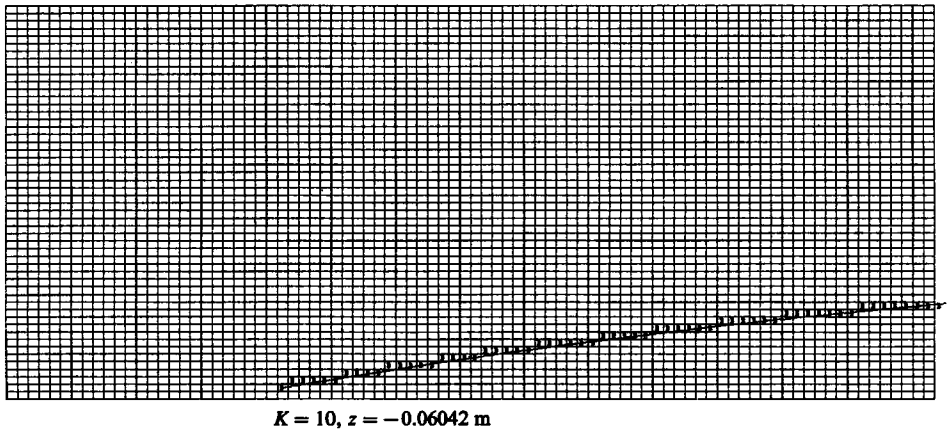

$K = 10$, $z = -0.06042$ m

FIGURE 10. Cell division of the forebody of a Wigley's hull on a (x, y)-horizontal plane.

this output can be utilized in many ways. The computational time (CPU time) was about 3 hours using a super-computer HITAC S-810/20.

The cell division of the practical ship form M55F0 in a lightly loaded condition is shown in figure 17 for the body surface and in figure 18 for a horizontal plane.

The computed wave-contour map at a steady state is shown in figure 19(*a*). Since

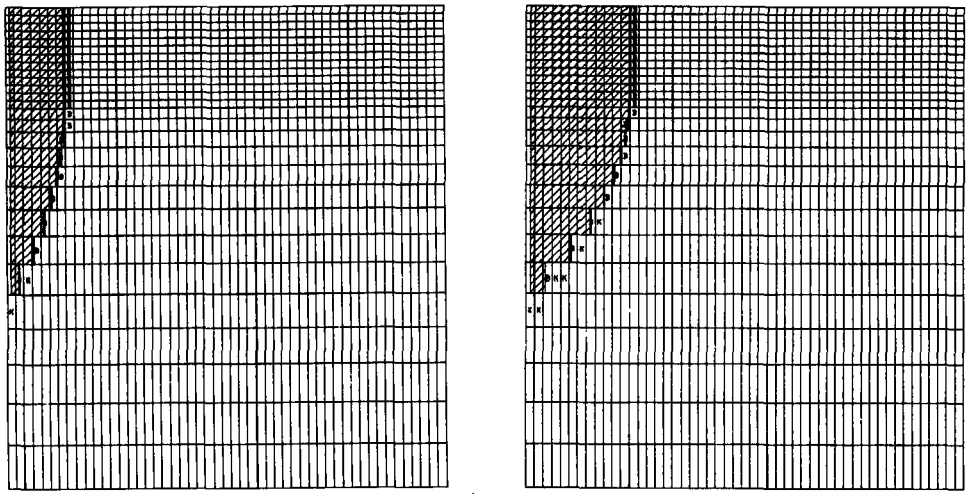

FIGURE 11. Cell division of the forebody of a Wigley's hull on two (y, z)-vertical planes.

the ship model M55F0 has a long parallel middle body, wave generation is concentrated near the two ends of the model. The details of bow and stern waves are shown in figure 19(*b*), (*c*) with smaller interval of contours. The foremost wave is most dominant showing steep wave slope, and the second crest has much smaller height and smaller angle of wave crest to the centreline. A steep wave is also generated from the rear end of the model, and it is spread to the rear far field by dispersion. Despite the complexity of the computed bow-wave system owing to the complicated body configuration with a bow bulb, the agreement with the measurements, shown in figure 20, is good. The computed wave profile on the hull surface of M55F0 is compared with the measured one in figure 21. The agreement is not so good as in the case of the Wigley's hull. In particular, the difference of phase and configuration of the second wave crest is noticeable. Its measured profile is somewhat similar to that of a deep-water bore having a small steep forward face, whereas the slope of the computed wave crest is much gentler. As is noted from the fact that the maximum wave height is about 80 % of the water head of the uniform stream, the nonlinearity of waves is much more conspicuous on this practical ship model having a complicated hull form with a blunt bow bulb. The approximate fulfilment of the exact free-surface and body-surface conditions of the present method seems to affect the solution of this case more significantly than the case of the very fine Wigley's hull.

Computed velocity-vector fields on vertical (y, z)-planes are shown in figures 22(*a*) and (*b*). Flow fields of the forebody are in figure 22(*a*) and of the afterbody in figure 22(*b*). Beneath the forebody a vortical motion of clockwise rotation appears and behind the afterbody one of anti-clockwise rotation. This vortex generation indicated by the present computation is in good qualitative agreement with the actual flow field. However, since a free-slip body boundary condition is employed in this computational procedure, it may be considered that these vortical motions are due to some numerical inaccuracy, despite the apparent agreement with experiment. The CPU time for this computation was about 4 hours and 50 minutes using a HITAC S-810/20, as the number of cells in which pressure is computed is about 100000.

The draught of the practical ship model M57F0 is divided into 6 cells on ballast

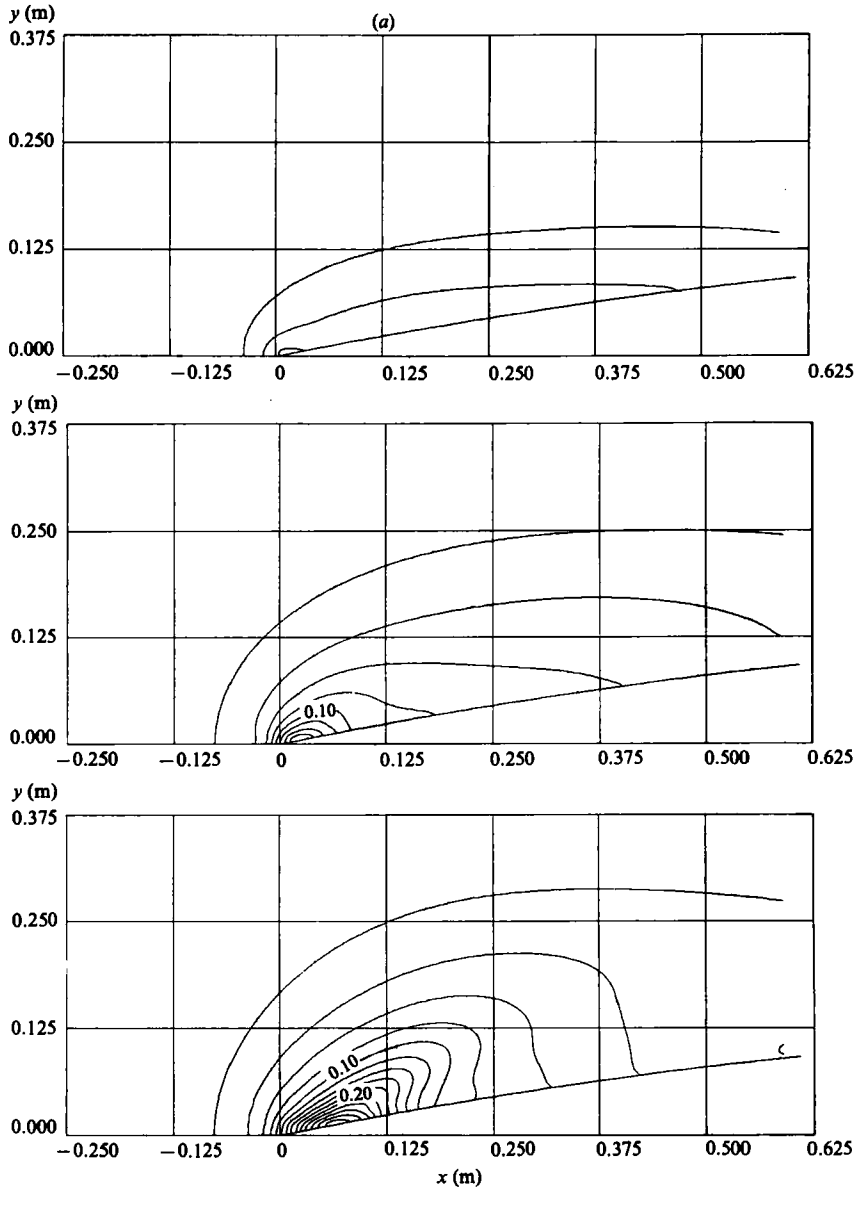

FIGURE 12(*a*). For caption see next page.

condition and 9 cells on full-load condition. Although the depth of the computational domain and the variation of cell spacing in the vertical direction is quite different between the two draught conditions, the cell spacing near the free surface and the total cell number are not very different, see table 2.

Although the Froude number based on the ship length *Fn* is common to the two conditions, the wave formation near the bow shows a remarkable difference as observed in figure 23, owing to the dependence on the Froude number based on draught, the importance of which is demonstrated by Miyata & Inui (1984). The pictures show that the forward face of the foremost wave is steeper and breaking

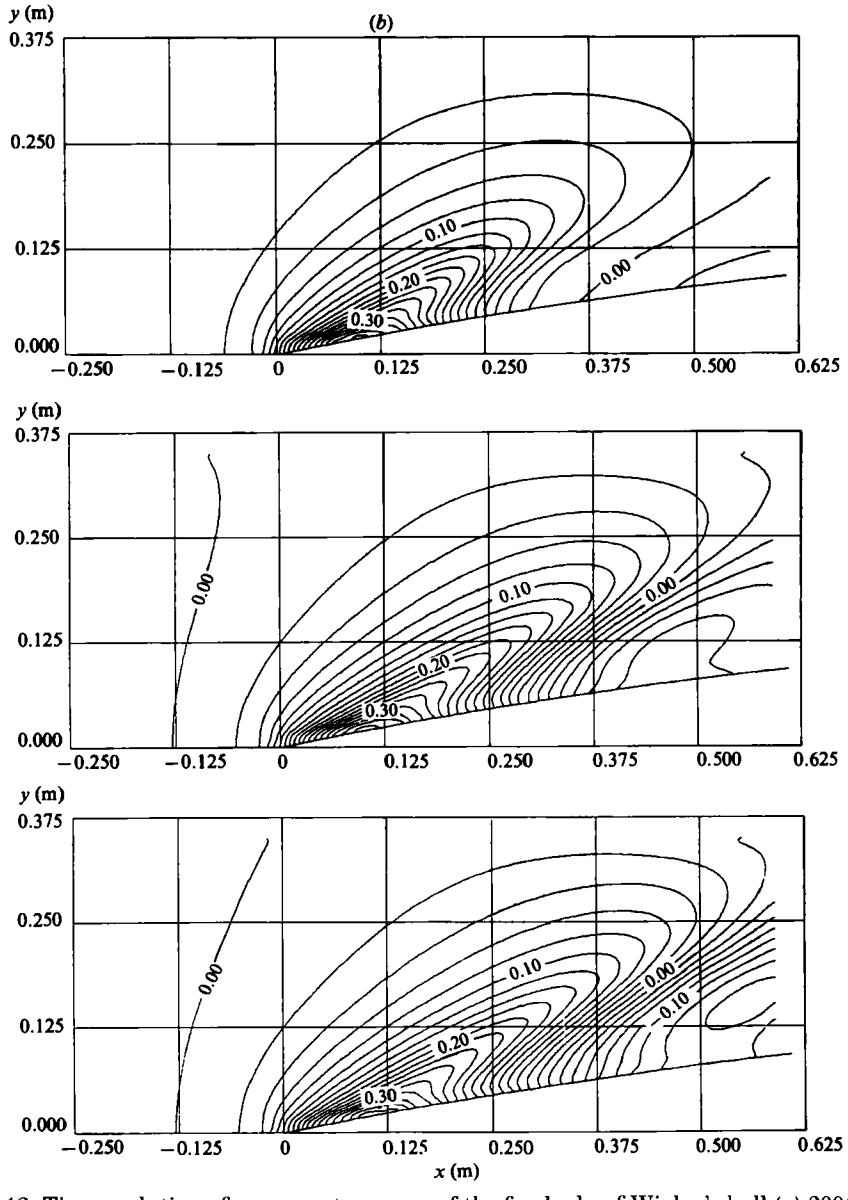

FIGURE 12. Time evolution of wave-contour map of the forebody of Wigley's hull (*a*) 200th, 300th and 400th time step from above. The interval of contours is $0.02H$ ($= U^2/2g$). (*b*) 500th, 600th and 700th time step. The uniform stream velocity is accelerated till the 500th time step, $Fn = 0.289$.

motions are obvious with the ballast condition, and that the second wave crest is generated only with the ballast condition. Waves are relatively gentle with the full-load condition. These qualitative differences in wave formation between the two draught conditions, except for the breaking motion, are well simulated by the present method as seen in the computed perspective views in figure 24.

The computed wave-contour maps at two time levels are compared with the measured ones in figure 25 for the ballast condition and in figure 26 for the full-load

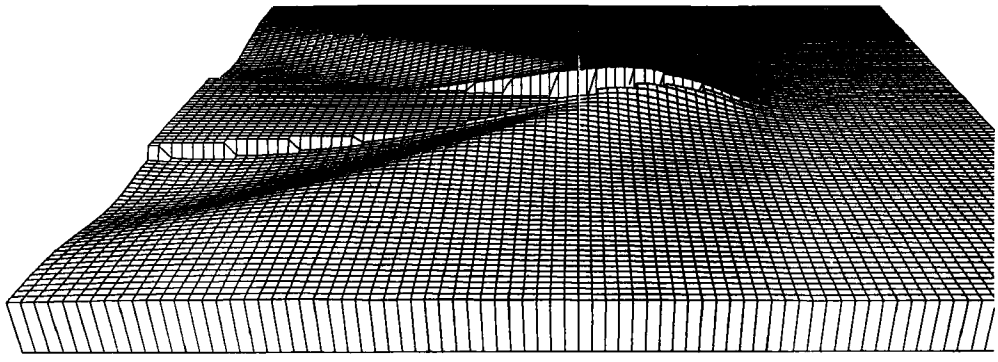

FIGURE 13. Perspective view of waves around the forebody of a Wigley's hull at $Fn = 0.289$, 700th time step.

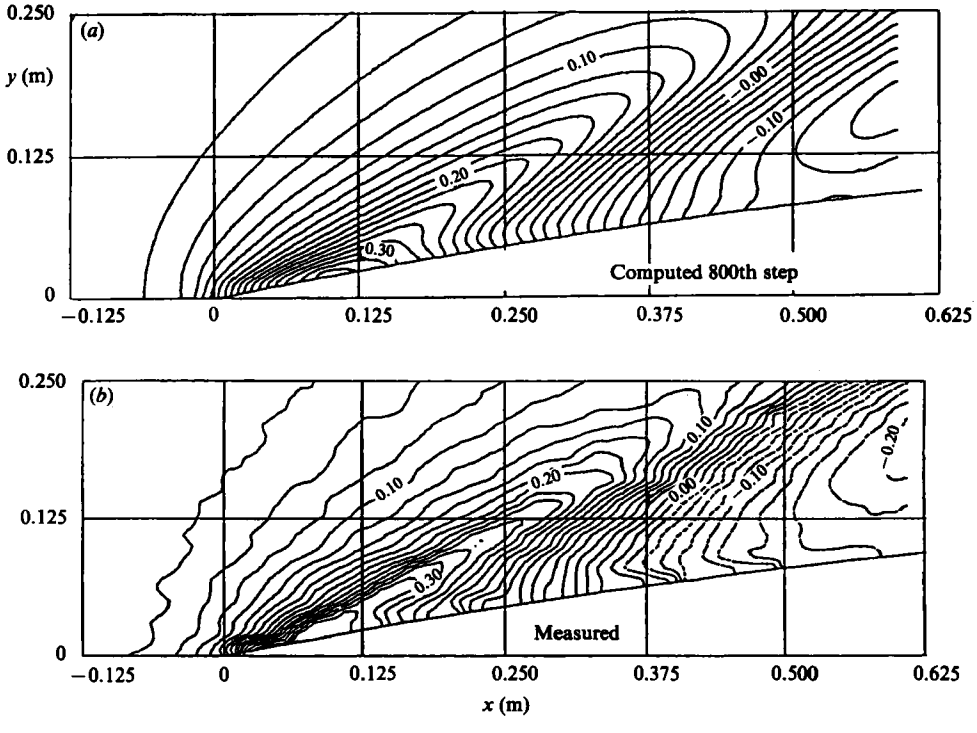

FIGURE 14. Comparison of (*a*) computed (800th time step) and (*b*) measured wave-contour maps of the forebody of a Wigley's hull at $Fn = 0.289$. The interval of contours is $0.02H$.

condition. The overall agreement is fairly good. It is noted that the degree of agreement for the full-load condition is more satisfactory than for the ballast condition. The computed maximum wave height of the foremost wave crest around the fore end is slightly higher than the measurement for the ballast condition, while it is slightly lower for the full-load condition.

In order to examine the discrepancy between computation and measurement in detail some wave profiles are compared in figures 27 and 28 for ballast condition and in figures 29 and 30 for full-load condition. The wave profiles were measured by a

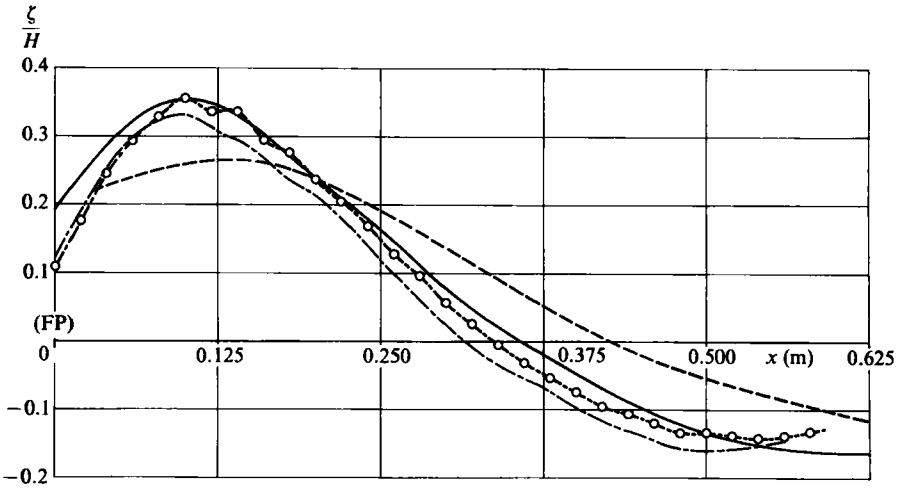

FIGURE 15. Comparison of wave profiles on the hull surface of the forebody of a Wigley's hull at $Fn = 0.289$; ——, measurement; --○--, present computation ($DX \times DY \times DZ = 10 \times 7 \times 6.3 \sim 35.4$ mm); —·—, computation with a little coarse cell ($DX \times DY \times DZ = 25 \times 10 \times 8.9 \sim 58$ mm); ---, modified Rankine source method by Ogiwara (1983).

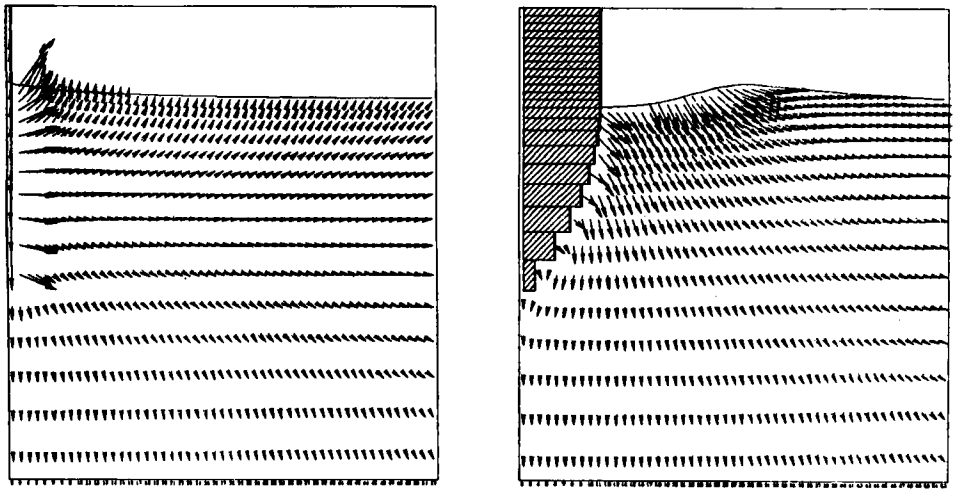

$I = 26$, $x = 0$ m $I = 64$, $x = 0.38$ m

FIGURE 16. Velocity vector field on (y, z)-vertical planes of the forebody of a Wigley's hull at $Fn = 0.289$.

FIGURE 17. Profile of cell division on the body surface of M55F0.

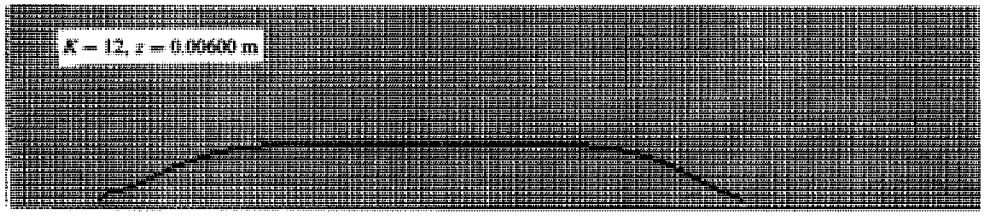

FIGURE 18. Cell division on a (x, y)-horizontal plane of M55F0.

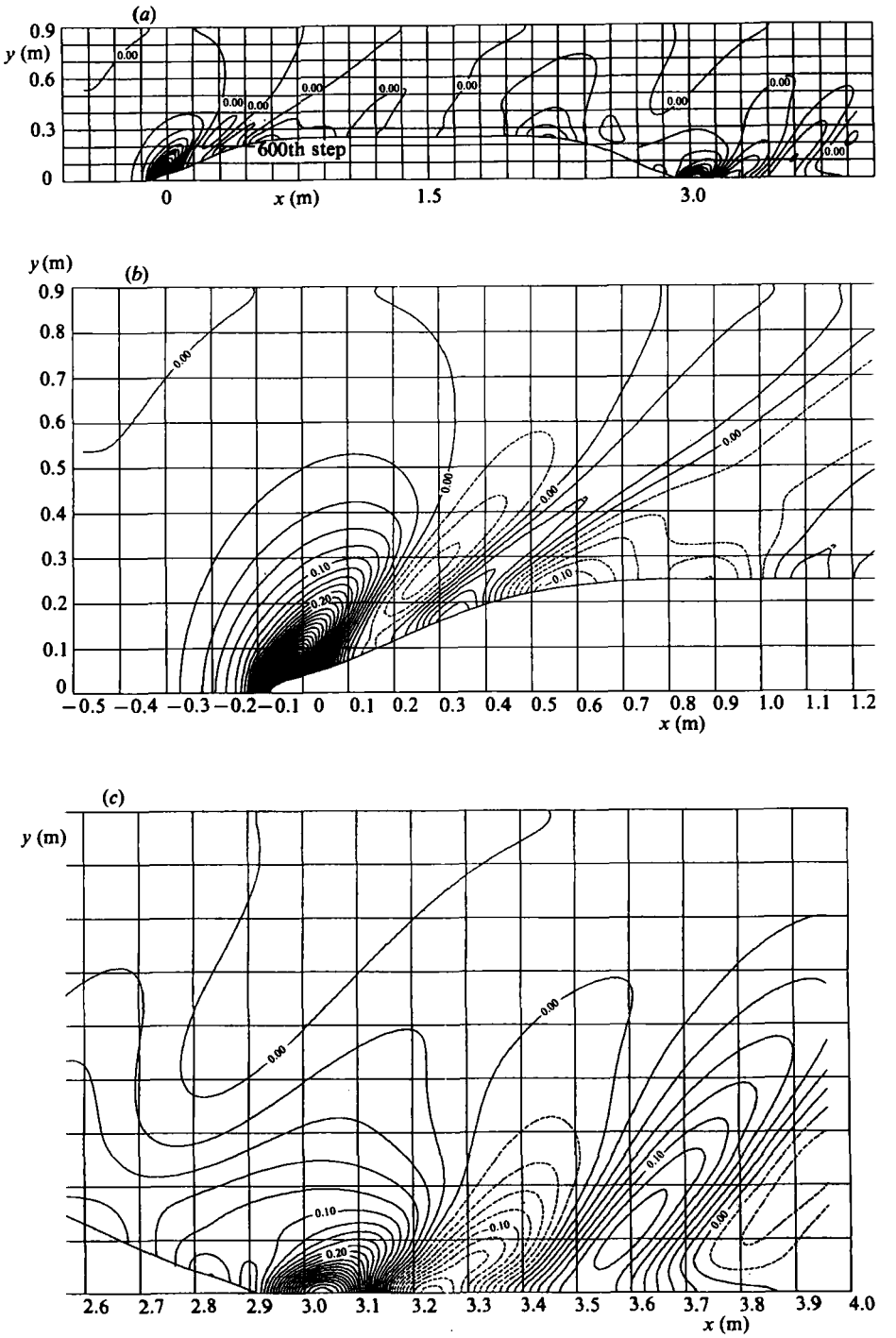

FIGURE 19. (*a*) Wave-contour map of M55F0 at $Fn = 0.180$, steady state at the 600th time step. The uniform stream is accelerated for 300 time steps. The interval of contours is $0.05H$. (*b*) Details of bow waves. The interval of contours is $0.02H$. Positive values are contoured by solid isopleths and negative values by dashed contours. (*c*) Details of stern waves. The interval of contours is $0.02H$.

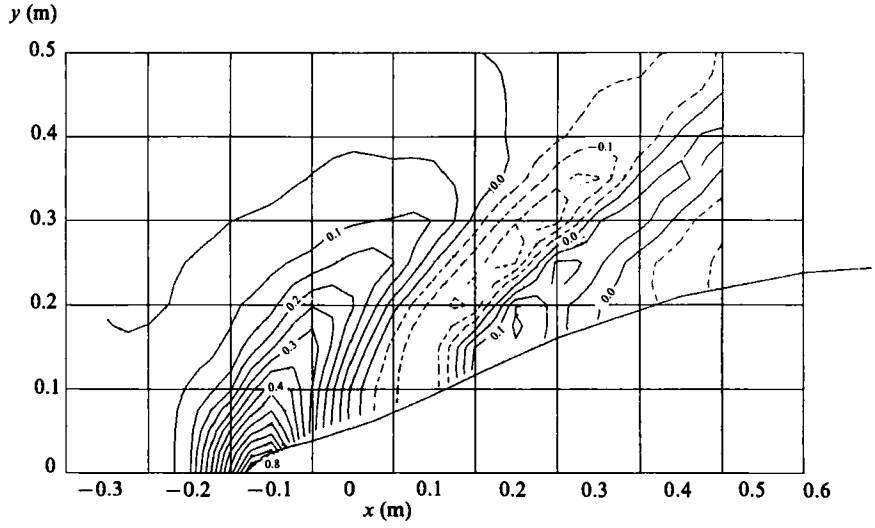

FIGURE 20. Measured wave-contour map of M55F0 at $Fn = 0.180$. The contour interval is $0.05H$. Positive values are contoured by solid isopleths and negative values by dashed contours.

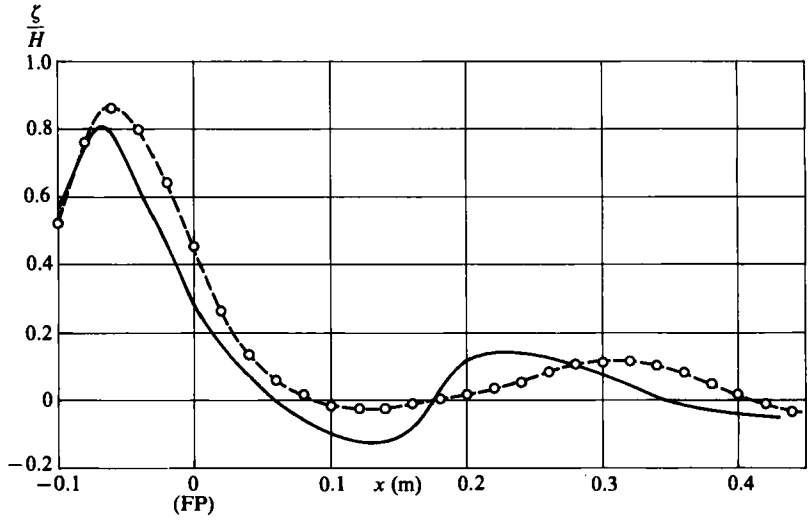

FIGURE 21. Comparison of wave profiles on the hull surface of the forebody of M55F0 at $Fn = 0.18$: ——, measurement; --○--, present computation.

contact-type wave recorder and the records from a pen-recorder are reproduced here. It is noted that the discrepancy for the ballast condition is most conspicuous where the wave profiles have high-frequency fluctuations and that these wave profiles with fluctuations show a jump-like shape which is considered to be some consequence of wave breaking. On the other hand the measured wave profiles for the full-load condition show a very small discrepancy, having gentler slope and relatively lower-frequency fluctuations which are attributed to the presence of capillary waves riding on the wave face and to the error in measurement. These comparisons indicate that the discrepancy is attributable not only to the numerical error but also to the breaking phenomenon which the present method cannot simulate.

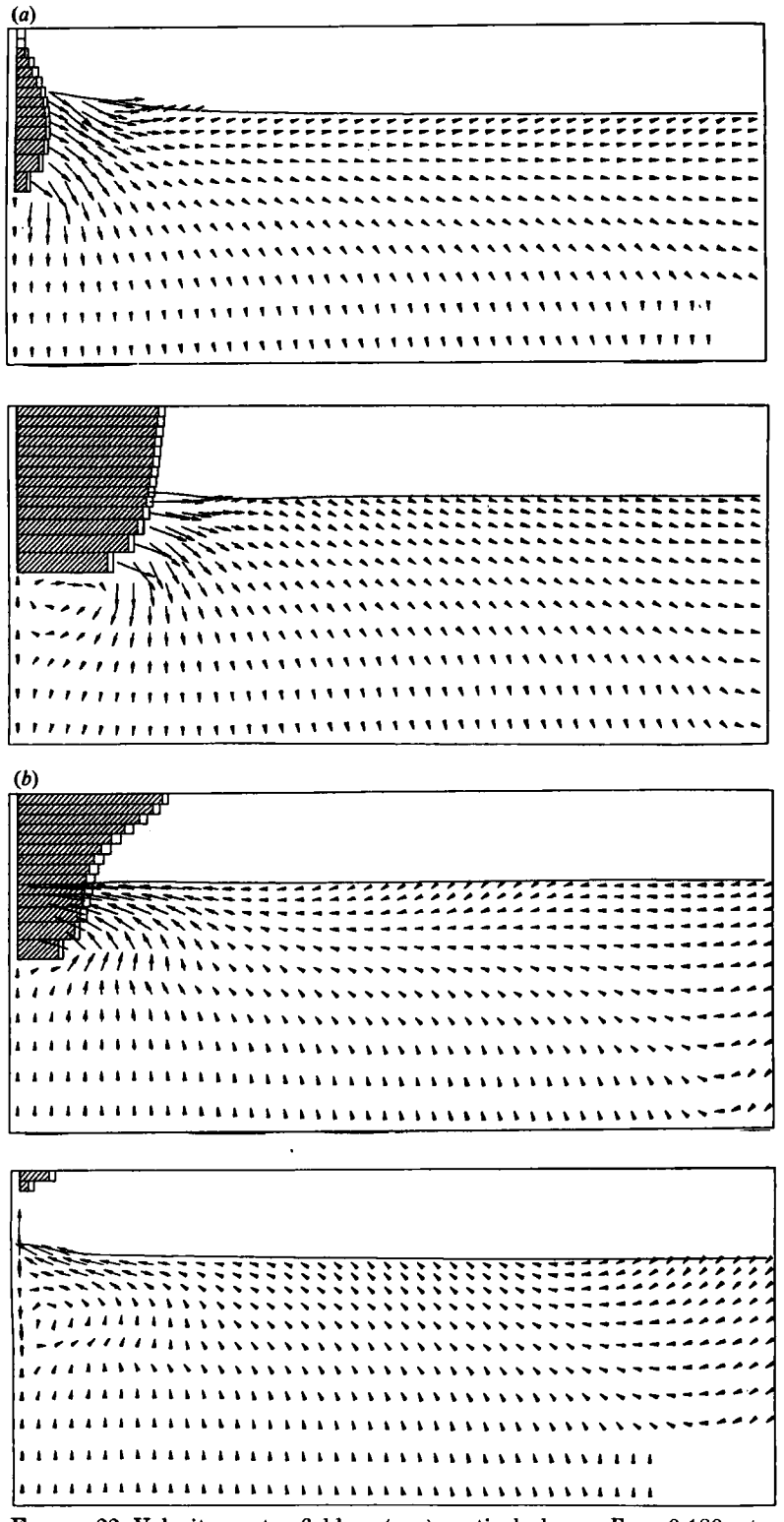

FIGURE 22. Velocity vector field on (y, z)-vertical planes, $Fn = 0.180$, at (*a*) $x = 0$ m and 0.3 m from above, (*b*) 2.7 m and 3.0 m.

(a)

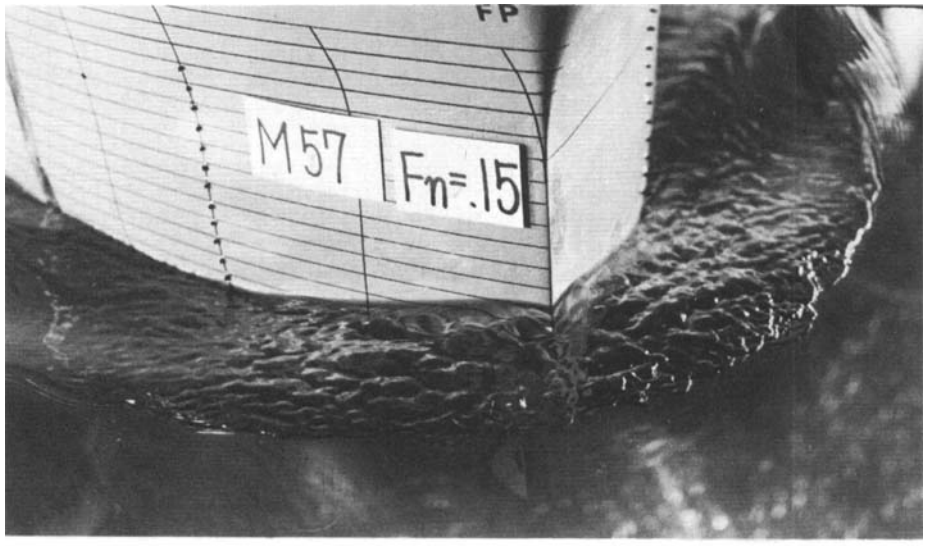

(b)

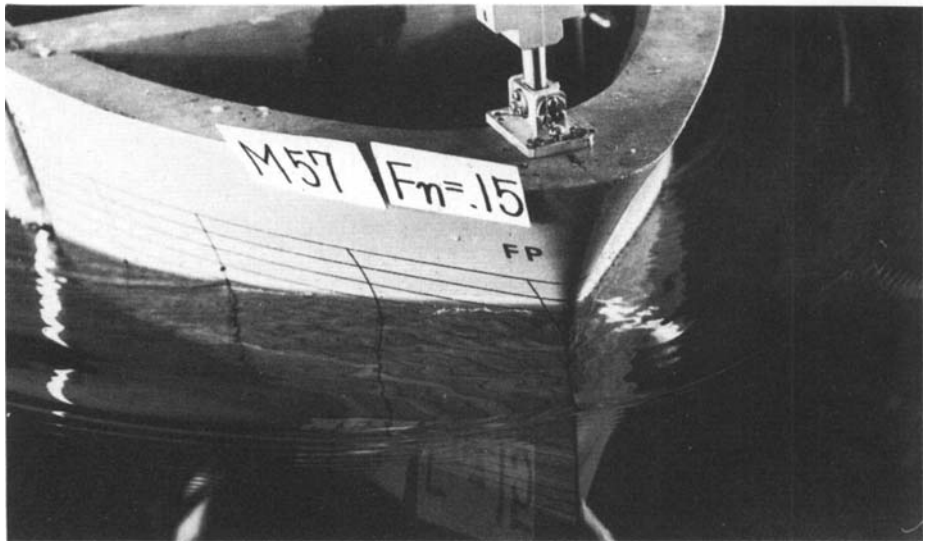

FIGURE 23. Bow-wave pictures of M57F0 at $Fn = 0.15$,
(*a*) ballast condition, (*b*) full-load condition.

The discrepancy in the formation of the second wave crest for the ballast condition seen in figure 25 is remarkable. Since wave breaking obviously occurs on the foremost wave crest at this higher Froude number based on draught, the flow field behind the breaking wave is assumed to be under the influence of the complicated free-surface motions caused by breaking involving free-surface turbulence. The inadequate agreement of the second wave is, at least partly, attributed to this secondary influence of the breaking phenomenon.

The CPU time was about 40 minutes for each condition. This is remarkably reduced

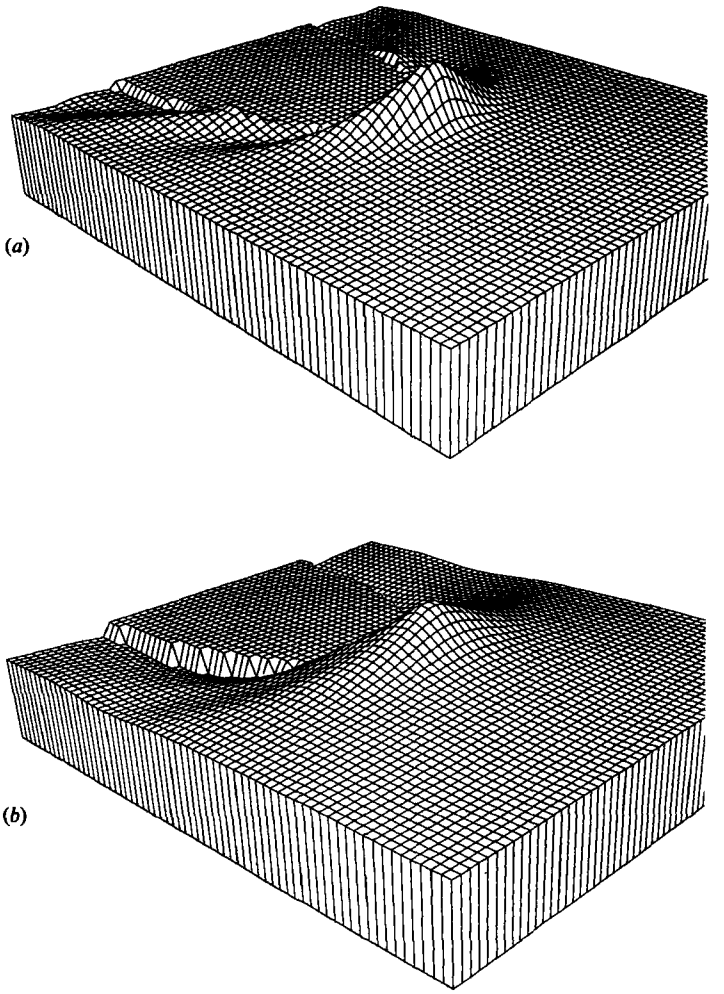

FIGURE 24. Perspective views of computed bow waves of M57F0 at $Fn = 0.15$, 800th time step, (*a*) ballast condition, (*b*) full-load condition. Wave height is four-times magnified.

in comparison with the aforementioned cases, mostly owing to the improvement of the optimization level of the compiler of the super-computer HITAC S-810/20 and to the reduction of iteration number in the solution procedure of the Poisson equation for the pressure.

3.3. *Discussion*

Fluid flow experiences abrupt changes in velocity and pressure near the ship body and this causes wave making. For a ship with a blunt bow at a certain high Froude number this change is so abrupt that steep waves are generated. They are usually the source of breakers and free-surface turbulence. In the region near the fore end of a ship where these waves are generated the linearizing assumption ceases to be valid, since the disturbance velocity by a ship approaches the value of the uniform stream with opposite sign and the wave height approaches the water head of the uniform stream. Therefore a numerical method of this kind will be particularly useful

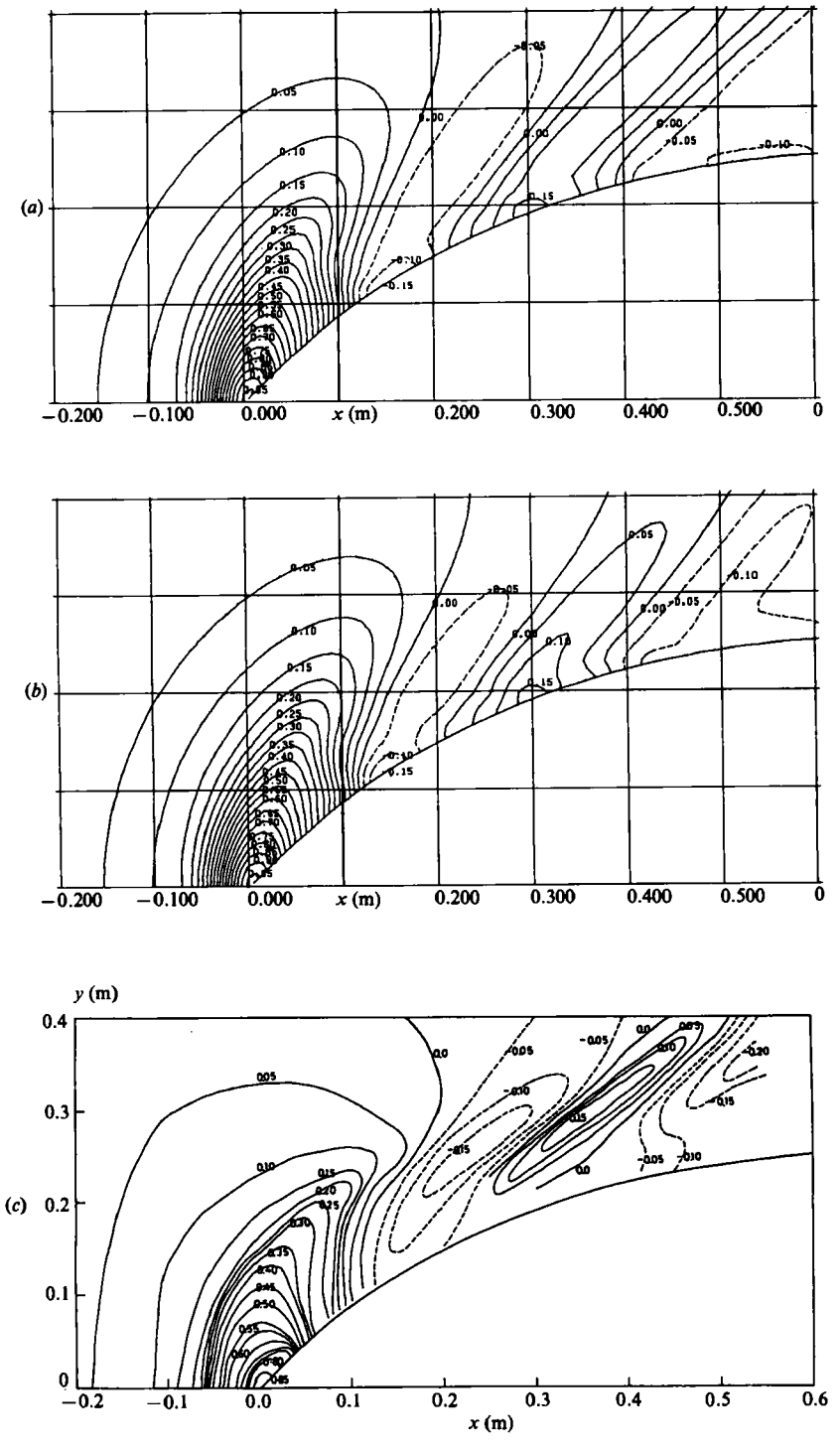

FIGURE 25. Comparison of computed and measured bow-wave contour maps of M57F0 on ballast condition at $Fn = 0.15$, (*a*) computed, 600th time step, (*b*) computed, 800th time step, (*c*) measured.

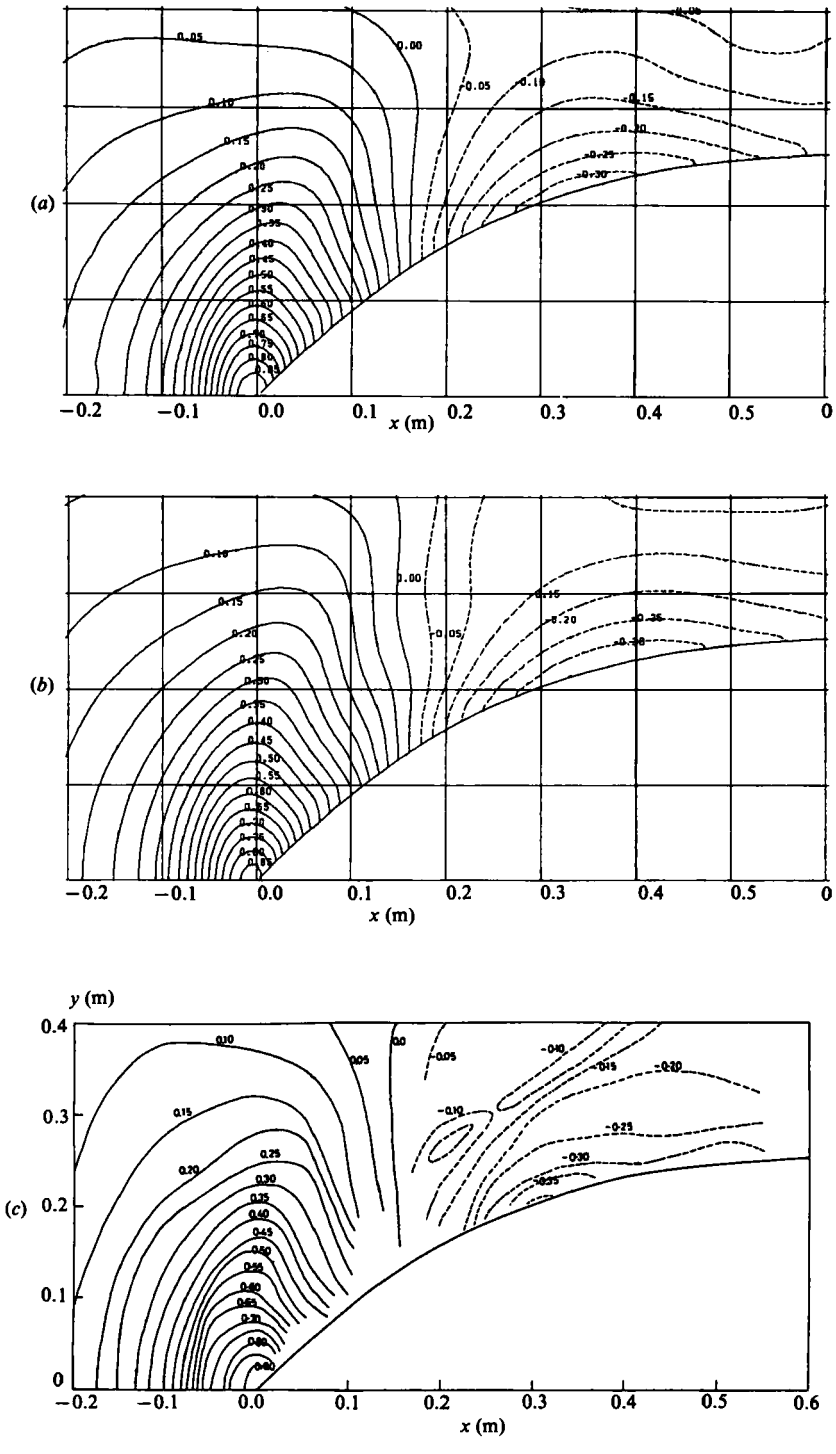

FIGURE 26. Comparison of computed and measured bow-wave contour maps of M57F0 on full-load condition at $Fn = 0.15$, (*a*) computed, 600th time step, (*b*) computed, 800th time step, (*c*) measured.

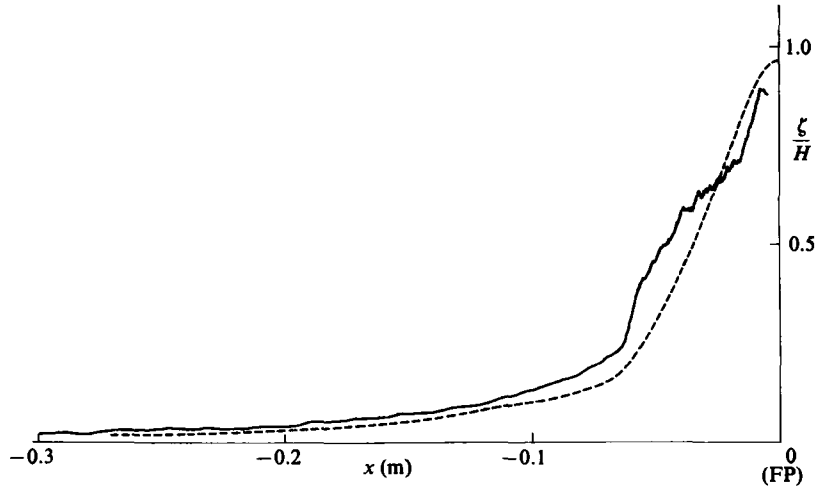

FIGURE 27. Comparison of wave profiles on the centreline of M57F0 on ballast condition at $Fn = 0.15$: ——. measured; ---, computed, 800th time step.

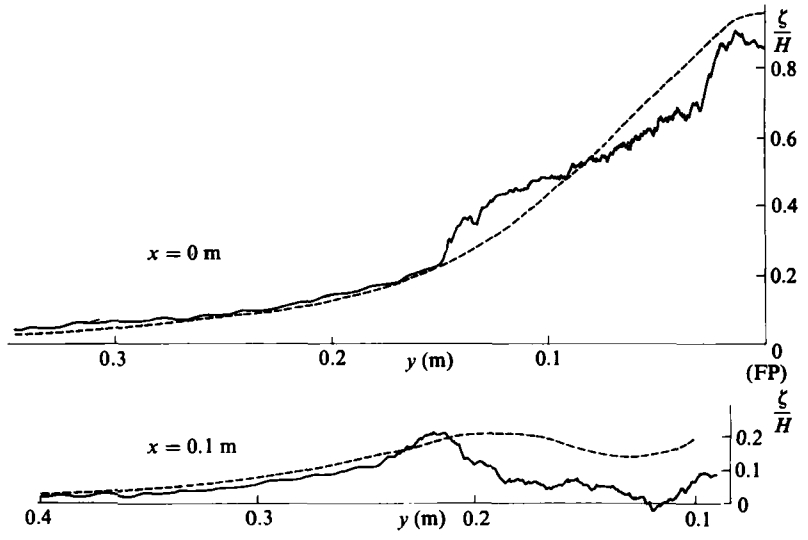

FIGURE 28. Same as figure 27, on two lateral lines.

in explaining waves around bows of low- and middle-speed ships with blunt bow configurations, since their bows are surrounded by water flow with large disturbance velocities and high wave elevation.

The computed waves of three hull forms show fairly good agreement with experimental results as demonstrated in the contour plots and the wave profiles. Although the approximate treatment of the body boundary condition within the framework of an inflexible rectangular-cell system is one of the shortcomings of this kind of method, the use of the variable-mesh system and the hybrid finite-differencing of the convective terms seems to be successful in overcoming the inaccuracy. The present method is expected to be effective for the development of improved hull forms having smaller wave resistance. However, further efforts should be made to increase

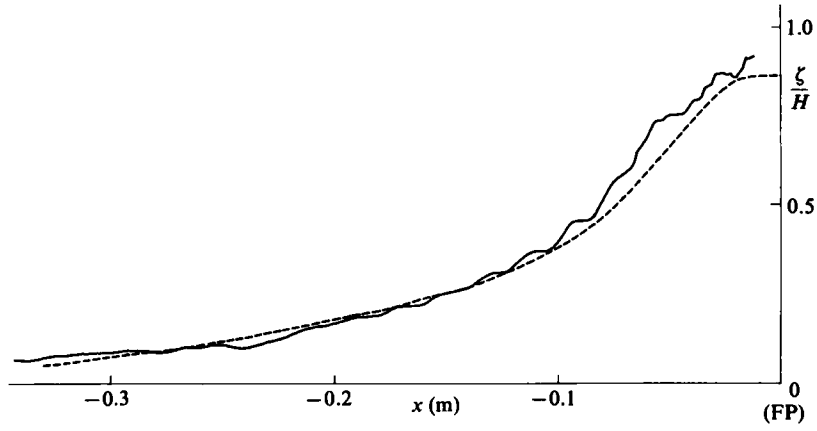

FIGURE 29. Comparison of wave profiles on the centreline of M57F0 on full-load condition at $Fn = 0.15$: ——, measured; – – –, computed, 800th time step.

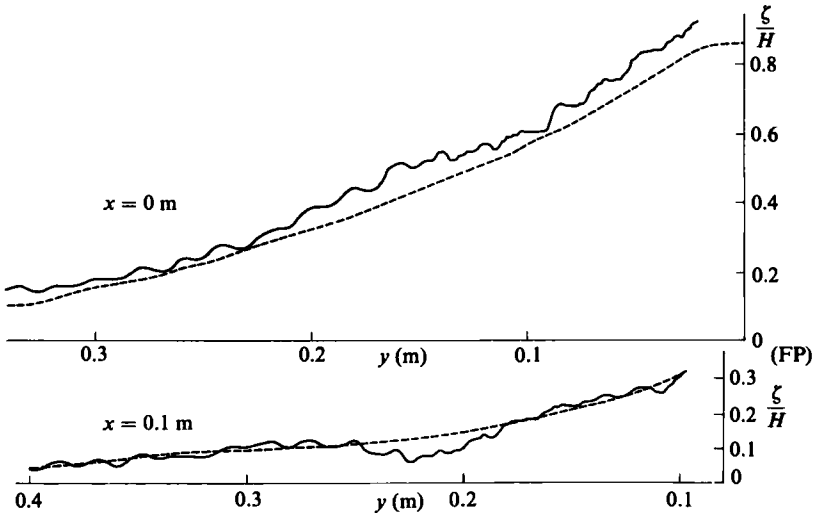

FIGURE 30. Same as figure 29, on two lateral lines.

the accuracy by improving the finite-difference scheme and by taking into account the more complicated nonlinear physical phenomena.

As is usually observed in a laboratory basin or in real oceans, ship waves in the near field are likely to break and free-surface turbulence occurs involving air entrainment. The characteristics of nonlinear ship waves in the vicinity of a ship have been experimentally studied by Miyata (1980) and Miyata & Inui (1984). The typical characteristics are (i) steepness of wave slope, (ii) systematic change of the angle of wave-crest line depending on Froude number, (iii) formation of lines of discontinuity sometimes with spilling or plunging breakers, (iv) turbulence generation on the wave crest and (v) dissipation of wave energy into momentum loss far behind. Because their characteristics and appearance are very similar to nonlinear shallow-water waves with discontinuity, the waves are called free-surface shock waves. The present computational method has, it is hoped, succeeded in explaining the characteristics

in the stages before energy-deficient phenomena take place. The simulation of breaking waves taking into account the free-surface turbulence will be the aim of future investigations.

Discussion of the comparison of predicted and measured values of the wave resistance coefficient has been avoided in this paper because the waves from the aft body and the pressure on the aft body owing to the waves are under the influence of the interaction of waves with a boundary layer and its separation, which cannot be interpreted by the present numerical method that employs a free-slip body boundary condition. Besides, wave resistance is very delicately evaluated by subtracting the high pressure on the aftbody from that on the forebody, that is, through cancellation of integrated pressure of the same order. In the test computation of the full length of the Wigley's hull, which is not included in this paper, the wave resistance coefficient made dimensionless with respect to the wetted-surface area is 1.259×10^{-3} at $Fn = 0.289$, while the measured value is 1.179×10^{-3}. The discrepancy is rather small for this fine hull form, on which the boundary-layer separation is not very conspicuous. However, for the full hull form M55F0, the predicted value is 1.747×10^{-3}, while the measured value is 0.617×10^{-3} at $Fn = 0.180$. In the flow field in the vicinity of the aft body the role of viscosity is important, and therefore a further advanced numerical method, that solves both wave motion and viscous boundary-layer motion simultaneously, must be developed to achieve satisfactory agreement in the values of resistance.

4. Concluding remarks

Ship waves that have markedly nonlinear characteristics are explained under inviscid nonlinear boundary conditions using a finite-difference method which is developed by synthesizing various techniques so far developed and developing new techniques that apply to the ship-wave problem in which the interaction of a uniform stream of large magnitude with a complicated configuration of hull form is of importance as well as the free-surface deformation.

The present finite-difference simulation method seems to have succeeded in explaining the generation of steep nonlinear waves before breaking. It can partly take the place of the experimental basin by using computer simulation of waves of forebodies of ships to discriminate a better hull form of smaller wave resistance from a series of configurations. For the establishment of a complete computational basin a lot of numerical techniques must be developed in order to explain breaking motion, viscous turbulence, ship motion and so forth.

The computations were undertaken by the super-computer HITAC S-810/20 of the Computer Centre, the University of Tokyo.

The authors are indebted to Professor H. Kajitani of the University of Tokyo, Mr A. Suzuki and Mr A. Masuko of Ishikawajima-Harima Heavy Industries, Mr K. Aoki of Kawasaki Heavy Industry and Dr T. Hino of Ship Research Institute for their valuable support and discussions. The authors also express a lot of thanks to Miss S. Nigo who has carefully typewritten the manuscript.

This research is partly supported by the Grant-in-Aid for Scientific Research of the Ministry of Education, Science and Culture and partly by the LINEC group of shipbuilders in Japan.

REFERENCES

BABA, E. 1969 A new component of viscous resistance of ships. *J. Soc. Naval Arch. Japan* **125**, 9–34.

CHAN, R. K.-C. & STREET, R. L. 1970 A computer study of finite amplitude water waves. *J. Comp. Phys.* **6**, 68–94.

DAGAN, G. & TULIN, M. P. 1972 Two-dimensional free-surface gravity flow past blunt bodies. *J. Fluid Mech.* **51**, 529–543.

DAWSON, C. W. 1979 Calculations with the *XYZ* free surface program for five ship models. *Proc. Workshop Ship Wave Resistance Computation*, DTNSRDC, pp. 232–255.

GADD, G. E. 1976 A method of computing the flow and surface wave pattern around full forms. *Trans. R. Inst. Naval Architects* **118**, 207–219.

HIRT, C. W. & NICHOLS, B. D. 1981 Volume of fluid (VOF) method for the dynamics of free boundaries. *J. Comp. Phys.* **39**, 201–225.

HIRT, C. W., NICHOLS, B. D. & ROMERO, N. C. 1975 SOLA-A numerical solution algorithm for transient fluid flows. *Los Alamos Scientific Lab. Report* LA-5852.

LIN, W. M., NEWMAN, J. N. & YUE, D. K. 1984 Nonlinear forced motions of floating bodies. *15th Symp. Nav. Hydrodynamics*, Hamburg.

MIYATA, H. 1980 Characteristics of nonlinear waves in the near-field of ships and their effects on resistance. *Proc. 13th Symp. Naval Hydrodynamics*, pp. 335–351.

MIYATA, H. & INUI, T. 1984 Nonlinear ship waves. *Adv. Appl. Mech.* **24**, 215–288.

NICHOLS, B. D. & HIRT, C. W. 1971 Improved free surface boundary conditions for numerical incompressible-flow calculations. *J. Comp. Phys.* **8**, 434–448.

OGIWARA, S. 1983 Numerical calculation of free surface flow by means of modified Rankine source method. *Proc. 2nd Workshop Ship Wave Resistance Computation*, DTNSRDC.

ROACHE, P. J. 1976 *Computational Fluid Dynamics.* Hermosa.

TANEDA, S. 1974 Necklace vortices. *J. Phys. Soc. Japan* **36–1**, 298–303.

VIECELLI, J. A. 1971 A computing method for incompressible flows bounded by moving walls. *J. Comp. Phys.* **8**, 119–143.

WELCH, J. E., HARLOW, F. H., SHANNON, J. P. & DALY, B. J. 1966 The MAC method. *Los Alamos Scientific Lab. Report* LA-3425.